Assessment of the Baseline Scenario at q_{95} ~ 3 for ITER

A.C.C. Sips[1,2], J. Schweinzer[3], T.C. Luce[4,9], S. Wolfe[5], H. Urano[6], J. Hobirk[3], S. Ide[6], E. Joffrin[7,11],

C. Kessel[8], S.H. Kim[9], P. Lomas[10,11], I. Nunes[12,11,9], T. Pütterich[3], F. Rimini[10,11], W.M. Solomon[4],

J. Stober[3], F. Turco[4,13], P.C. de Vries[9] and JET Contributors[11,a], the ASDEX Upgrade team[3,b], the DIII-D

team[4,c], the C-Mod team[5,d], the JT-60U team[6,e] and ITPA-IOS TG members and experts

[1] JET Exploitation Unit, Culham Science Centre, Abingdon OX14 3DB, UK.

[2] European Commission, Brussels, Belgium.

[3] Max-Planck-Institut für Plasmaphysik, Garching D-85748, Germany.

[4] General Atomics, San Diego, California, USA.

[5] Massachusetts Institute of Technology, Plasma Science and Fusion Center, Cambridge, Massachusetts, USA.

[6] National Institutes for Quantum Radiology Science and Technology, 801-1 Muko-yama, Naka, Ibaraki 311-0193, Japan.

[7] CEA, IRFM, F-13108 Saint-Paul-lez-Durance, France.

[8] Princeton Plasma Physics Laboratory, Princeton University, Princeton, New Jersey, USA.

[9] ITER Organization, Route de Vinon-sur-Verdon, CS 90 046, 13067 St. Paul lez Durance Cedex, France.

[10] CCFE, Culham Science Centre, Abingdon, Oxfordshire OX14 3DB, UK.

[11] EUROfusion Consortium, JET, Culham Science Centre, Abingdon, OX14 3DB, UK

[12] Instituto de Plasmas e Fusão Nuclear, IST, Universidade de Lisboa, Portugal.

[13] Columbia University, New York, NY, USA

e-mail contact of the main author: george.sips@jet.uk

Abstract

The International Tokamak Physics Activity (ITPA) topical group on Integrated Operational Scenarios (IOS) has compiled a database of stationary H-mode discharges at $q_{95} \sim 3$ from AUG, C-Mod, DIII-D, JET and JT-60U, for both carbon wall and high-Z metal wall experiments with ~ 3300 entries. The analyses focus on discharges that are stationary for ≥ 5 thermal energy confinement times to evaluate the baseline scenario proposed for ITER at 15 MA for achieving its goals of Q = 10, fusion power of 500 MW at normalised pressure, $\beta_N = 1.8$ and normalised confinement as predicted by the standard H-mode scaling, $H_{98y2} = 1$. With the data restricted to stationary H-modes at $q_{95} \sim 3$, the database shows significant variation of thermal energy confinement compared to the standard H-mode scaling (IPB98(y,2)) in dimensionless form. The data show similar scaling with normalised gyro-radius, but more favourable scaling towards lower collision frequency and more favourable scaling with plasma beta. Using all the engineering variables employed in IPB98(y,2), results in an overfit due to correlations among the data. Moreover, there are significant residual trends in the confinement for plasma current, device size, loss power, and in particular for the plasma density. Significant differences between results obtained for devices with a carbon wall and high-Z metal wall are observed in the data, with data from carbon wall devices providing a larger operating space, encompassing ITER parameters or even exceeding them. H-modes in high-Z metal wall devices have, so-far, not accessed conditions at low collision frequencies, have lower normalised confinement ($H_{98y2} \sim 0.8$ to 0.9) at low input power or beta, achieving $H_{98y2} \sim 1.0$ only at input powers two times the L- to H-mode transition scaling predictions and at $\beta_N \sim 2.0$. Hence, only the best H-modes with high-Z metal walls reach ITER baseline performance requirements. The data show that operating at high plasma density, with line-averaged density at 85 % of Greenwald density is achievable for $H_{98y2} > 0.95$ for a range of plasma configurations, and that operation at low plasma inductance with $l_i(3) \sim 0.7 - 0.75$ is feasible. Scenario simulations employed for projecting the plasma performance in ITER should incorporate a lower thermal confinement at low plasma beta for the entry to burn and provide projections using higher levels of plasma core radiation by plasma impurities. Moreover, ITER

pρojections should not subtract the core radiation in the evaluation of the thermal confinement time and H_{98y2}, to allow a fair comparison with experimental data currently available. From the data presented here, it is likely that in ITER the energy confinement time will not increase with plasma density and will have no degradation with plasma beta. The analyses indicate that the data at $q_{95} \sim 3$ are consistent with achievement of the ITER mission goals at 15 MA.

1. Introduction

The ITER Research Plan (IRP) [1] addresses its main mission goals: 1) to obtain plasma dominated by α-particle heating, 2) to produce a significant fusion gain (Q ≥ 10), and 3) to achieve steady-state operation of a tokamak at Q ≥ 5 for a pulse length up to 3000 s. The basic operational scenarios proposed [2] include the baseline or reference scenario, which targets fusion gain Q ~ 10 using a conventional ELMy H-mode discharge at 15 MA plasma current and a toroidal field of 5.3 T (with a safety factor at 95 % flux, q_{95} = 3). The ITER Research Plan allows programme logic to be developed and key operational challenges to be identified and addressed during construction while exploring the issues in burning plasma physics likely to be encountered on route to Q ~ 10 using the baseline scenario. In this respect, obtaining maximum information from experiments and supporting simulations is essential in preparing for ITER operation.

During the last decade, many experiments have been performed on devices with different first wall components. Metallic wall components, like those planned for ITER, have been tested, ranging from a few tungsten (W) tiles in the divertor in ASDEX Upgrade (AUG) in the mid-1990's [3] and in JT-60U [4 and references therein], to full tungsten coverage in AUG [5] and a molybdenum wall in Alcator C-Mod (C-Mod) [6, 7]. JET has tested an ITER-Like Wall configuration with Be walls and a W divertor [8]. Other experiments have continued to use full graphite coverage, DIII-D in particular [9]. The results from AUG, C-Mod, DIII-D, JET and JT-60U provide insight to the differences in operation and the results obtained in preparing ITER operating scenarios. Important is that data are

taken for plasma operation near q_{95} ~ 3, as trends observed at different (mainly higher) q_{95} would need to be confirmed for the operation domain planned for ITER.

The currently recommended ELMy H-mode energy confinement time scaling [10], derived from a regression on a multi-machine database and generally referred to as IPB98(y,2), is

$$\tau_{IPB98(y,2)}[s] = 0.0562 \; P_{loss}^{-0.69} \; B_0^{0.15} \; I_p^{0.93} \; \kappa_a^{0.78} \; n_e^{0.41} \; a^{0.58} \; R_{geo}^{1.39} \; M^{0.19} \tag{1}$$

where $P_{loss} = P_{in} - dW_{th}/dt$ is the power loss from the plasma by conduction or convection, not subtracting the plasma core radiation, $\kappa_a = S_{area}/(\pi a^2)$ is a measure of the plasma elongation, n_e is the line averaged electron density (in 10^{19} m^{-3}), M is the isotope mass normalised to the mass of a proton, P_{in} is the sum of the ohmic and auxiliary power (P_{aux}) coupled to the plasma, W_{th} is plasma thermal energy, "a" and R_{geo} are the minor and major radius of the plasma and S_{area} is the poloidal cross-sectional plasma area. The confinement quality H_{98y2} is the thermal energy confinement time (τ_{th}) normalised to the scaling relation given in Eq (1).

The Integrated Operation Scenarios Topical Group of the ITPA (ITPA-IOS TG) has coordinated experiments in H-mode at q_{95} ~ 3 in several tokamak devices (AUG, C-Mod, DIII-D, JET and JT-60U) that can be compared to simulations of ITER operation at Q ~ 10 (baseline scenario). Validation of the ITER scenario reported in [11] showed that plasma breakdown at ITER values for E_{axis} < 0.23 -0.33 V/m is possible and that for the current ramp up, good control of the plasma inductance is obtained using a full-bore plasma shape with early X-point formation [12, 13, 14]. Additional heating during the current rise phase can keep the plasma inductance $l_i(3)$ < 0.85 while H-mode transition is possible during the current rise phase. The principal aim of joint experiments reported here was to demonstrate stationary operation at q_{95} = 3, β_N = 1.8 and f_{GW} ≤ 0.85, matching the main plasma and performance parameters in the ITER simulations, with f_{GW} being the ratio of line averaged electron density and the Greenwald H-mode density limit (n_{GW}) [15]. The results of these joint experiments are combined with other data available at q_{95} ~ 3 from the five devices involved in this study, to

review and document the operating space explored up to the end of 2014 and to provide a widest possible range of parameters such as input power, plasma density and beta.

The paper has the following outline: Section 2 gives the details of the ITER baseline scenario. The scalar (0-D) database for the studies presented in this paper is given in section 3, detailing which devices contributed to the study, the range of parameters obtained in the experiments, the time-period over which the data were obtained and the material of the first wall. The experimental data are complemented with simulations for ITER operation at Q ~ 10 at 15 MA. In section 4, the dimensionless parameter space and trends of confinement with dimensionless variables are reviewed for the experiments at q_{95} ~ 3, indicating scaling with normalised Larmor radius and collisionality, together with 'gaps' in the operating space compared to ITER. In section 5, the data are compared to confinement scaling laws using dimensionless and engineering parameters. The plasma confinement properties of the experiments with beta and plasma density are given in section 6, focussing on the difference between data from devices with carbon wall and all metal walls. In section 7, the range of input powers and radiation levels are compared to the power required to achieve H-mode. In section 8, the operating space in terms of plasma beta and plasma inductance is reviewed, together with the potential fusion performance of baseline experiments when projected to ITER. In section 9, the results obtained are discussed and recommendations for further studies are given. The main conclusions of the paper are given in section 10.

2. The ITER baseline scenario

Several performance metrics will be used both for comparison among present-day tokamak results and projections to ITER. The normalised pressure $\beta_N \equiv (\langle p \rangle / \langle B^2 \rangle)/(I_p/aB_0)$ is the pressure normalised to a theoretical scaling that describes well the ideal MHD stability limit of a free-boundary plasma in the absence of a wall [16]. Here p is the plasma pressure, B_0 is the vacuum toroidal magnetic field at the geometric centre of the plasma, I_p is the plasma current (in MA), and a

is the minor radius of the plasma (in MKS units except where noted). The ITER baseline scenario envisions operation at β_N = 1.8. A value of H_{98y2} = 1 is used to estimate the performance of the ITER baseline scenario. ITER requires robust operation of various plasma scenarios within the hardware constraints of the device. Operation in H-mode at 15 MA and nominal value for q_{95} = 3 is planned to achieve 500 MW fusion power at Q = 10 with plasma densities at 85 % of the Greenwald density limit. Using the IPB98(y,2) confinement scaling, the margins for the design point at 15MA for achieving ITER's goals can be explored as summarised in table I; the plasma performance is computed using H_{98y2} = 1.0 and f_{GW} = 0.85 and a summary is given for I_p = 15 MA (reference point), I_p = 13.5 MA and I_p = 16.5 MA at fixed additional heating power of 50 MW. Operation below 15 MA, but at fixed f_{GW}, would reduce the stored energy of the D-T plasma more than linearly with plasma current, i.e. with $I_p^{1.34}$ [10]. Moreover, the reduction in stored energy would reduce the fusion power, and heating of the plasma, further reducing the stored energy by $P_{loss}^{0.31}$. On the other hand, if operation at 16.5MA is possible, the fusion power and alpha heating would significantly increase at H_{98y2} = 1 or 500MW of fusion power would still be achievable for H_{98y2} = 0.88.

I_p [MA]	15	13.5	16.5
q_{95}	3[1]	3.33	2.73
f_{GW}	0.85	0.85	0.85
n_e x 10^{19} [m^{-3}]	10	9	11
$W_{th}/(W_{th}$ at 15MA)	1.0	0.80	1.26
β_N	1.8	1.6	2.06
P_{fus} [MW]	500	317	791
P_{heat} [MW] (including α-heating)	150	113	208
Q_{fus}	10	6.33	15.8
H_{98y2} required to obtain P_{fus}= 500 MW	1.0	1.15	0.88

Table I: Variation of ITER baseline performance at 15 MA, 13.5 MA and 16.5 MA at fixed Greenwald fraction f_{GW} = 0.85. Assuming β_N = 1.8, P_{fus} = 500 MW and Q = 10 at 15 MA. IPB98(y,2) scaling with H_{98y2} = 1 is used to compute values for 13.5 MA and 16.5 MA, using 50 MW additional heating. [1]: The q_{95} values in the two simulations provided for ITER range from 2.85 to 3.27.

The normalised beta of the plasma (β_N) would decrease at lower plasma current due to the decrease in alpha power, while β_N would increase from 1.8 at 15 MA to 2.06 at 16.5 MA, despite being at higher plasma current compared to the reference scenario. The fusion gain, Q, would drop to 6.3 at I_p = 13.5 MA (q_{95} = 3.33), unless the confinement is increased to H_{98y2} = 1.15. For operation at I_p = 16.5 MA (q_{95} = 2.73), Q would rise to nearly 16, if H_{98y2} = 1.0 can be obtained.

For ITER, an optimised scenario for the 15 MA baseline has been designed including the entry to burn, flat-top burning plasma operation and exit from burn. Variants with different current ramp-up and ramp-down times, as well as different heating waveforms are possible. For the simulations used in this paper, the plasma is initially an inboard limited configuration and assumed to quickly grow to be diverted around t = 12 s, the plasma current is ramped up to 15 MA at t = 60 s. The current flat-top is assumed to end at t = 500 s. The plasma current is then ramped down relatively slowly compared to the ramp-up phase, to avoid instabilities associated with the high plasma internal inductance. During the ramp-down phase, the plasma stays in a diverted configuration while it is slowly moving downward, reducing plasma elongation. This CORSICA simulation from 2015 [17] uses the reference plasma shape for ITER and has q_{95} = 3.27, β_N = 1.9, H_{98y2} = 1.03, giving Q = 9.5 and using Be/Ar impurities to obtain Z_{eff} = 1.7, the simulation results are given in Figure 1.

Another baseline simulation is available from 2013 using the DINA code [18]; this simulation is aimed at achieving the longest possible burn phase within the limitations of the poloidal field coils. During the flat-top phase at 15 MA q_{95} = 2.86 is achieved, which is lower compared to the CORSICA simulation results shown in Figure 1, by reducing the plasma cross-section to provide more Volt-seconds for the flat-top phase of the simulation. A normalised beta β_N of 1.8 is obtained with H_{98y2} set at 1.0, giving a fusion gain Q of 10.2. In these simulations carbon is the main impurity giving Z_{eff} = 1.7.
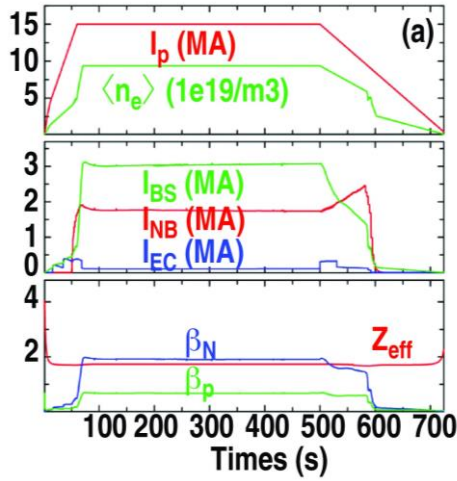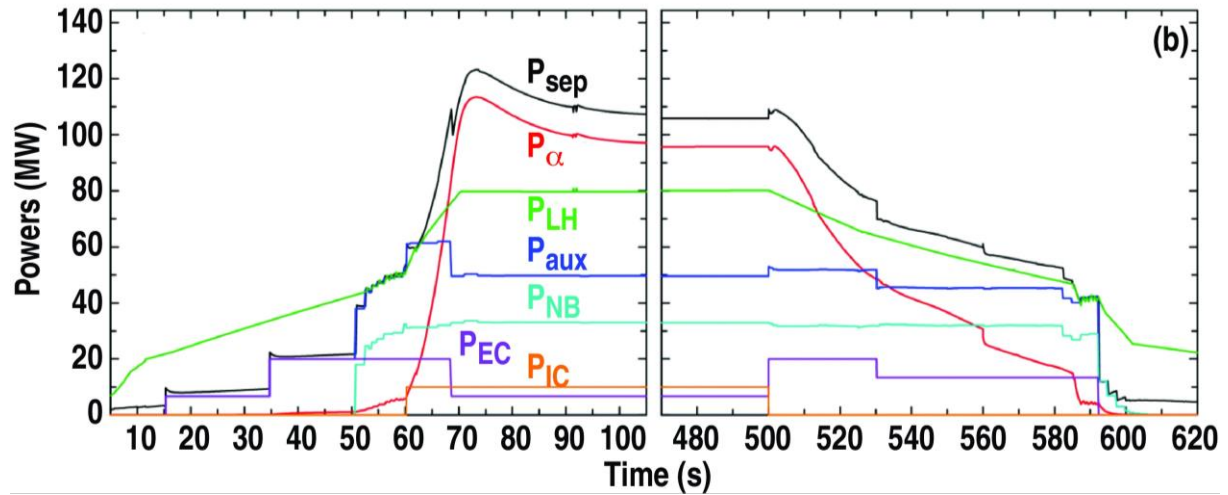
Figure 1: ITER baseline simulation. (a) From top to bottom: Time traces of the plasma current (I_p), volume averaged electron density (<n_e>), bootstrap current (I_{BS}), NB and EC driven currents (I_{NB} and I_{EC}), effective charge number (Z_{eff}), and normalised and poloidal plasma betas (β_N and β_p). For current ramp-up (b) with H-mode access, and for current ramp-down (c) with H-L transition, time traces of the power crossing the separatrix (P_{sep}), alpha particle self-healing power (P_{alpha}), H-mode threshold power estimate (P_{LH}), total auxiliary heating power (P_{aux}) and NB/EC/IC power (P_{NB}, P_{EC}, P_{IC}) are shown. The simulations are based on work published in [17].

3. Database for stationary discharges with q_{95} = 2.7 - 3.3

A database with global parameters has been assembled by the ITPA-IOS TG for deuterium discharges that have q_{95} in the range 2.7 to 3.3 (i.e. q_{95} = 3 ± 10 %) from AUG, C-Mod, DIII-D, JET and JT-60U using both carbon wall and (high-Z) metal walls. Note that for all experiments the data supplied are up to 2014 only, allowing publication of the latest results by the individual experiments and organisations first, in-line with ITPA practice. The data available from the experiments are summarised in Table II. Note that the colour code used for the different tokamak devices is used in overview plots throughout the paper, whenever results from machines are compared.

— For ASDEX Upgrade (AUG), operation with some carbon plasma facing components ended in 2006, followed by operation with full tungsten walls from 2008 onwards. Data are available from both periods starting in 1998. ITER demonstration discharges at triangularity δ ~ 0.36 are included. With the tungsten wall, careful programming of gas dosing and central heating with ICRH or electron cyclotron heating (ECH) are required to obtain stationary discharges at q_{95} ~ 3. In Figure 2a an example is given of a stationary H-mode at AUG at q_{95} ~ 3. Discharges at q_{95} ~ 3.6, reported in [19] are not included in the dataset.

— For Alcator C-Mod (C-Mod), operating with molybdenum walls, discharges with ion cyclotron resonance heating (ICRH) > 1 MW are selected for diverted plasmas with elongation (κ) > 1.5. The discharges are from the period 2009 to 2012 and include H-mode and I-mode discharges. Compared to H-modes, I-mode discharges do not have a density pedestal at the edge of the plasma [20, 21, 22] and are achieved with the ion $B \times \nabla B$ drift away from the X-point. The C-Mod data contain ITER demonstration discharges at both 2.7 T and 5.4 T, matching the ITER shape [13]. An example of an H-mode discharge from C-Mod is given in Figure 2b, showing that radiation excursions limit the stationary period during the heating phase at low q_{95} in C-Mod. To note is that in C-Mod H-mode discharges are not usually ELMy and stationary discharges have enhanced D_{α} activity (EDA) or are ELM-free.

— Data from DIII-D with carbon plasma facing components are available for the period 1996 to 2014. The dataset contains a large number (1059) of discharges with different plasma shapes, including demonstration discharges matching the ITER shape and discharge evolution [23]. DIII-D has data at q_{95} ~ 3 with different heating schemes using co-neutral beam injection (NBI), counter-NBI, ICRF heating and ECRH, allowing variations of ion/electron heating and the applied torque to the plasma. An example with neutral beam heating only, is given in Figure 2c.
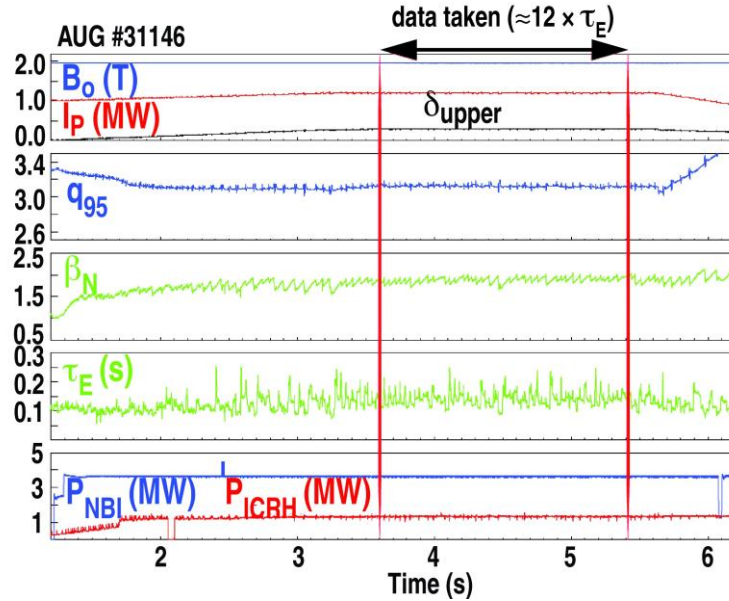
Figure 2a: A discharge in AUG at q₉₅ ~ 3 with the full tungsten wall. From top to bottom the toroidal field (in T) in blue, plasma current (in MA) in red, q₉₅ in blue, β_N in green, energy confinement time (in seconds) in green, neutral beam power (in MW) in blue and ICRH power (in MW) in red. The time window for which the data are averaged to provide an entry for the database is indicated.
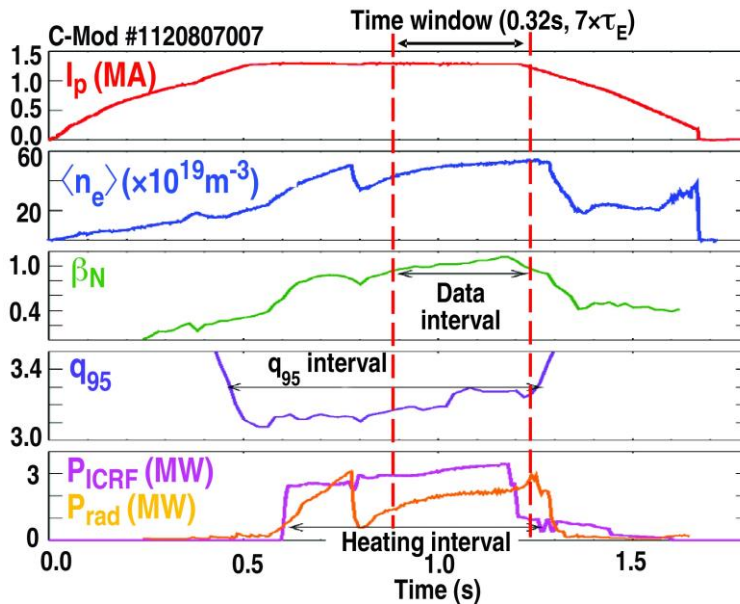

Figure2b: An H-mode discharge in C-Mod at q₉₅ ~ 3. From top to bottom the plasma current (in MA) in red, line averaged electron density in blue (in units of 10¹⁹m⁻³), β_N in dark green, q₉₅ in purple, ICRH power (in MW) in magenta and radiated power (in MW) in orange. The time window for which the data are averaged to provide an entry for the database is indicated.
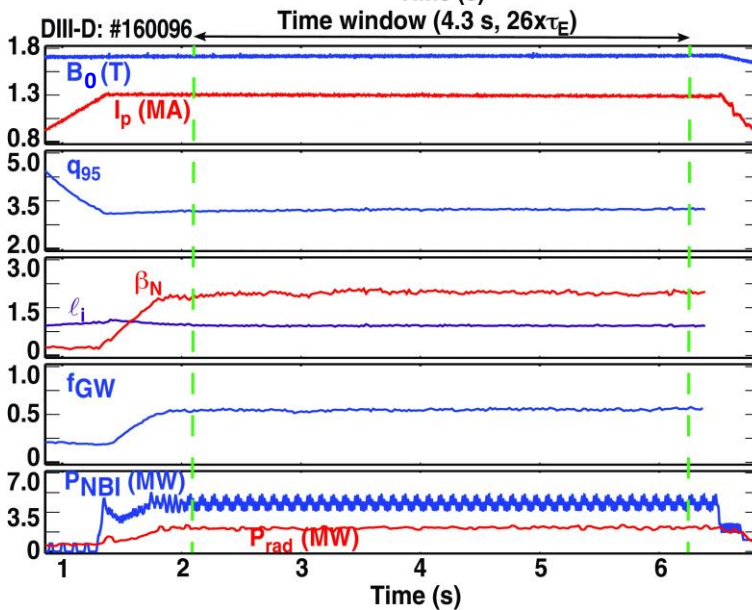

Figure 2c: A demonstration discharge at q₉₅ ~ 3 in DIII-D. From top to bottom the plasma current (in MA) in red, the toroidal field (in T) in blue, q₉₅ in blue, β_N in red, the plasma inductance (l_i) in purple, the Greenwald density fraction in blue, neutral beam power (in MW) in blue, ICRH power (in MW) in red and radiated power (in MW) in red. The time window for which the data are averaged to provide an entry for the database is indicated.
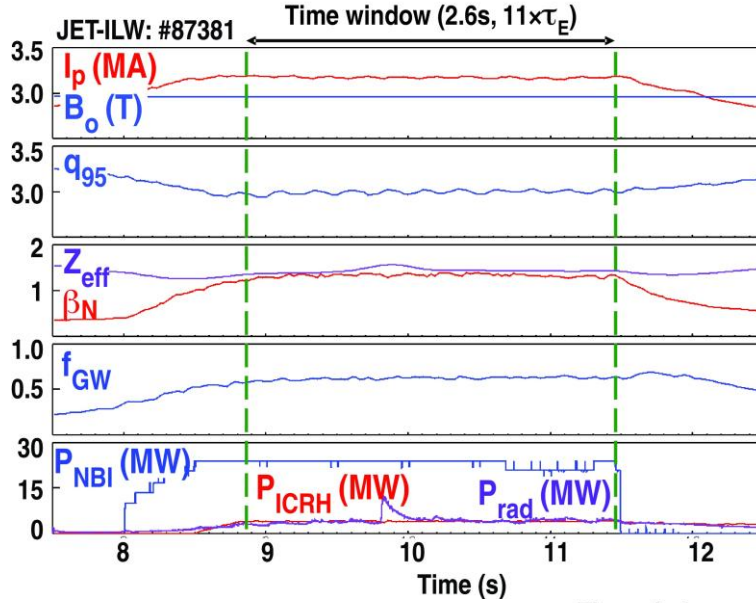
Figure 2d: JET discharge at q$_{95}$ = 3 with the ITER-like Wall. From top to bottom the plasma current (in MA) in red, the toroidal field (in T) in blue, q$_{95}$ in blue, β_N in red, Z$_{eff}$ in purple, the Greenwald density fraction in blue, neutral beam power (in MW) in blue, ICRH power (in MW) in red and radiated power (in MW) in purple. The time window for which the data are averaged to provide an entry for the database is indicated.
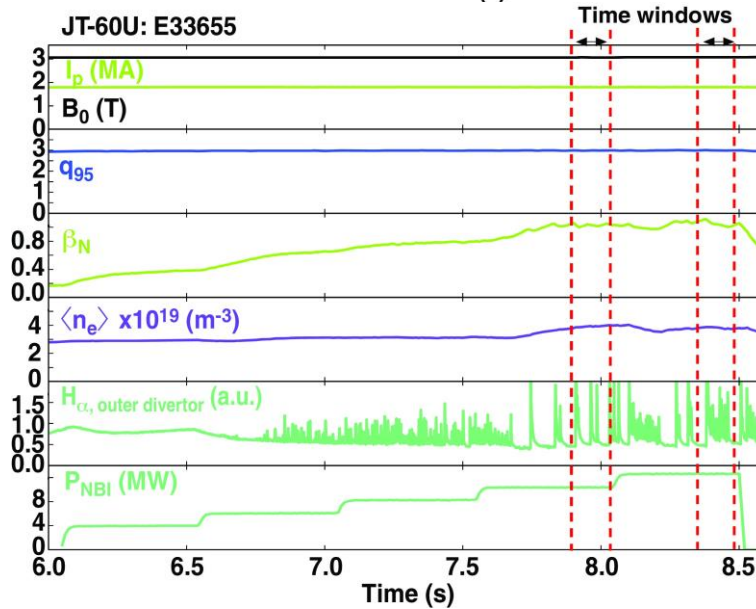

Figure 2e: A JT-60U discharge at q$_{95}$ ~ 3. From top to bottom the plasma current (in MA) in green, the toroidal field (in T) in black, q$_{95}$ in blue, β_N in green, line-averaged electron density in purple (in 10^{19} m^{-3}), H-alpha signal in green and neutral beam power (in MW) in green, which has five levels in this discharge. The time windows for which the data are averaged to provide an entry for the database are indicated.

− JET operates routinely at q$_{95}$ ~ 3 with dominant NBI heating. Operation with carbon walls ended in 2009. H-mode data with an ITER-like beryllium wall and a tungsten divertor are available since 2012 [24, 25]. An example is given in Figure 2d. With a large amount of data available, only discharges with constant plasma density are selected for JET.

− For JT-60U, results with carbon walls are available. The data come from dedicated neutral beam power scans at q$_{95}$ ~ 3 performed in 1999, with several steps in NBI power (~ 1 s) during the discharge [4], as shown in Figure 2e. With the total energy confinement time (τ_E) in the range 0.23

s to 0.46 s, the data supplied are the parameters achieved at the end of these heating steps (several time windows per discharge).

Device	Wall	Entries		Period [year]	I_p [MA]	B_0 [T]	P_{NBI} [MW]	P_{ICRH} [MW]	P_{EC} [MW]	n_e [10^{19}m^{-3}]	f_{GW}	H_{98y2}
AUG CFC	Some CFC	191	*Min*	1998	0.8	1.4	0	0	0	2.1	0.22	0.6
			Max	2006	1.2	2.3	12.5	6.4	1.1	12.4	0.91	1.5
AUG W-wall	W	47	*Min*	2008	1.0	1.7	2.2	0	0	7.9	0.59	0.7
			Max	2014	1.2	2.0	7.3	2.6	2.6	14.3	1.00	1.1
C-Mod H-mode	Mo	61	*Min*	2009	0.6	2.6		0.8		10.4	0.19	0.5
			Max	2012	1.3	5.4		3.6		59.1	0.84	1.0
C-Mod I-mode	Mo	97	*Min*	2009	1.0	4.2		1.6		9.0	0.12	0.6
			Max	2012	1.4	5.7		4.2		21.0	0.28	1.1
DIII-D Carbon	C	1059	*Min*	1996	0.6	0.6	0	0	0	1.3	0.11	0.5
			Max	2014	2.0	2.2	15.5	1.3	3.5	11.7	1.13	1.5
JET CFC	CFC	1237	*Min*	2000	1.0	1.0	0	0		2.0	0.24	0.5
			Max	2009	4.0	3.6	22.9	10.4		33.9	1.24	1.5
JET ITER-like Wall	Be/W	617	*Min*	2012	1.4	1.3	1.1	0.0		2.9	0.40	0.6
			Max	2014	4.0	3.7	25.9	5.4		9.5	1.09	1.2
	CFC	31	*Min*	1999	1.8	3.1	5.9		0	2.4	0.30	0.7
			Max	1999	1.8	3.1	10.6		0	4.5	0.53	1.1
ITER, Q=10	Be/W	2	*Values*	2013	15.0	5.3	26.6	0	20.0	10.0	0.80	1.00
			Values	2015	15.0	5.3	33	10	6.7	9.6	0.83	1.03

Table II. *Overview of the entries in the database. For ITER, P_α ~ 100 MW. CFC denotes a first wall made from Carbon Fibre Composite tiles, W-Wall implies a first wall full covered by tungsten tiles in ASDEX Upgrade, the ILW in the JET stand for ITER-Like Wall composed of beryllium first wall tiles and tungsten (coated) divertor tiles. DIII-D uses first wall tiles made from fine-grain graphite (carbon). In Alcator C-Mod the discharge categories are divided in H-mode and I-mode discharges.*
*: Colour coding used for the different devices in some of the overview plots given in this paper.

The data from the experiments and ITER simulations (presented in section 2) are averaged for the period when $\beta_N \geq 0.85\,\beta_{N,max}$, where $\beta_{N,max}$ is the maximum normalised beta during the pulse. The analyses are restricted to discharges that are stationary for duration ≥ 5 τ_E during the heating phase. An exception to this rule are the data provided by JT-60U, with data provided during a power scan during the discharge, with power steps after the plasma reaches stationary conditions. Spanning > 15 years of data, ~ 3300 entries of stationary discharges have been collected; most of the data (75 %) are from discharges with carbon walls (AUG, DIII-D, JET-CFC and JT-60U) as summarised in Table II. Data from C-Mod with a shorter duration (< 5 τ_E) are also available as well as I-mode data;

these data can be used to confirm trends seen in the data. Examples of discharges submitted to the database are given in Figures 2a-c, for AUG, C-Mod, and JET-ILW.

The parameter variation in the database is given in Table II and in Figure 3 below. The data cover a wide range of plasma conditions in plasma current (0.6 MA to 4 MA), toroidal field (0.6T to 5.75T), line averaged electron density (1.3×10^{19} m^{-3} to 6.0×10^{20} m^{-3}) as well as a wide range of plasma shaping parameters, κ = 1.5 to 2.0 and δ_x = -0.15 to 0.8, with κ the elongation at the plasma boundary and δ_x the average triangularity at the plasma boundary. Normalised parameters achieved are H_{98y2} = 0.55 - 1.55, β_N = 0.55 - 3.8 and f_{GW} = 0.15 to 1.15, containing a much larger operating space than foreseen for ITER.

Most of the data lie in the range I_p = 1 − 2 MA and only JET provides data up to 4 MA. C-Mod has data at the highest toroidal field values with H-mode entries up to B_o = 5.7 T, close to the ITER toroidal field value for Q ~ 10 operation. Most discharges lie in the range q_{95} = 3 - 3.3, with only few data entries for q_{95} < 3, mainly from JET. AUG results with the carbon wall and DIII-D provide entries to the database that are well distributed around H_{98y2} ~ 1 as do data from JET-CFC. For the all metal devices: (1) C-Mod entries for H-modes have H_{98y2} below 1, (2) also most of the JET-ILW wall data have H_{98y2} values below 1 and (3) AUG-W confinement values are on average just below H_{98y2} = 1. There is a significant difference for devices in the values for the line averaged density normalised to the Greenwald density (f_{GW}). DIII-D and JT-60U have all data entries for f_{GW} < 0.6. There is a significant split in f_{GW} values between I-mode and H-mode operation in C-Mod, reflecting the lower particle confinement for I-mode discharges. Both AUG and JET have a large range for f_{GW}, however data for all tungsten walls in AUG and beryllium-tungsten walls in JET are typically at f_{GW} ~ 0.8.

The variation of the discharge parameters in the database provides an opportunity to explore parameter dependencies for H-mode operation at q_{95} ~ 3 and where possible draw conclusions for ITER baseline operation. When data from carbon wall devices are plotted together in this paper, the data from carbon wall devices are given using grey symbols and experiments with metal walls are

displayed in red. When the data from carbon wall devices and high-Z wall devices are shown separately, the devices are marked with different colours as indicated in Table II and Figure 3.
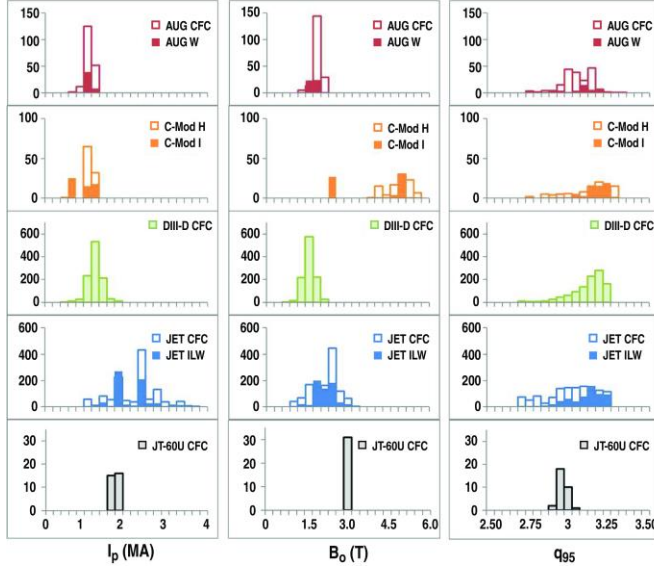

Figure 3a: For five tokamaks (from top to bottom: AUG, C-Mod, DIII-D, JET and JT-60U) the variation is given for plasma current (left panels), the absolute value of the toroidal field (middle panels) and the range for q_{95} (right panels). The y-axis gives the number of entries. For AUG and JET, the results obtained with CFC walls (open bars) and metal walls are overlaid (closed bars). For C-Mod, the data include H-mode (closed bars) and I-mode discharges (open bars).
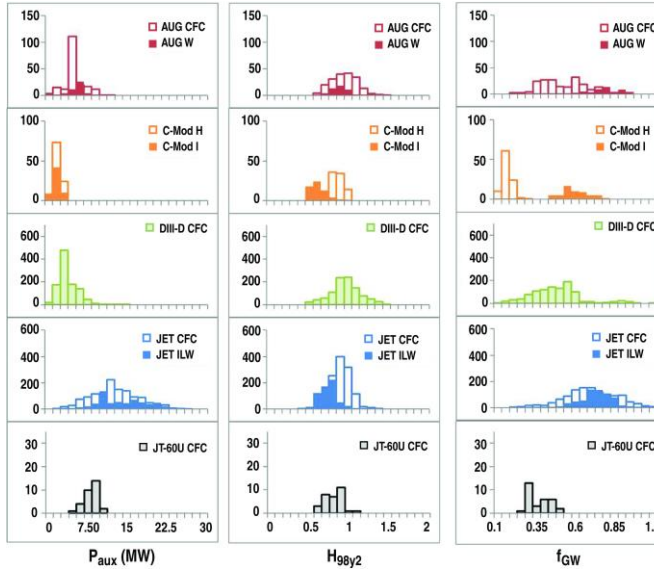

Figure 3b: For five tokamaks (from top to bottom: AUG, C-Mod, DIII-D, JET and JT-60U) the variation is given for total auxiliary heating power in MW (left panels), the normalised energy confinement H_{98y2} (middle panels) and the range for Greenwald fraction (f_{GW}) obtained in the discharges (right panels). The y-axis gives the number of entries. For AUG and JET, the results obtained with CFC walls (open bars) and metal walls are overlaid (closed bars). For C-Mod, the data include H-mode (closed bars) and I-mode discharges (open bars).

4. Dimensionless parameter space and confinement trends

As described in section 3, the assembled dataset at q_{95} = 2.7 to 3.3 show variation in the energy confinement normalised to the standard H-mode confinement scaling, indicating possible

deficiencies in the scaling coefficients used, or influence of additional physics variables absent from

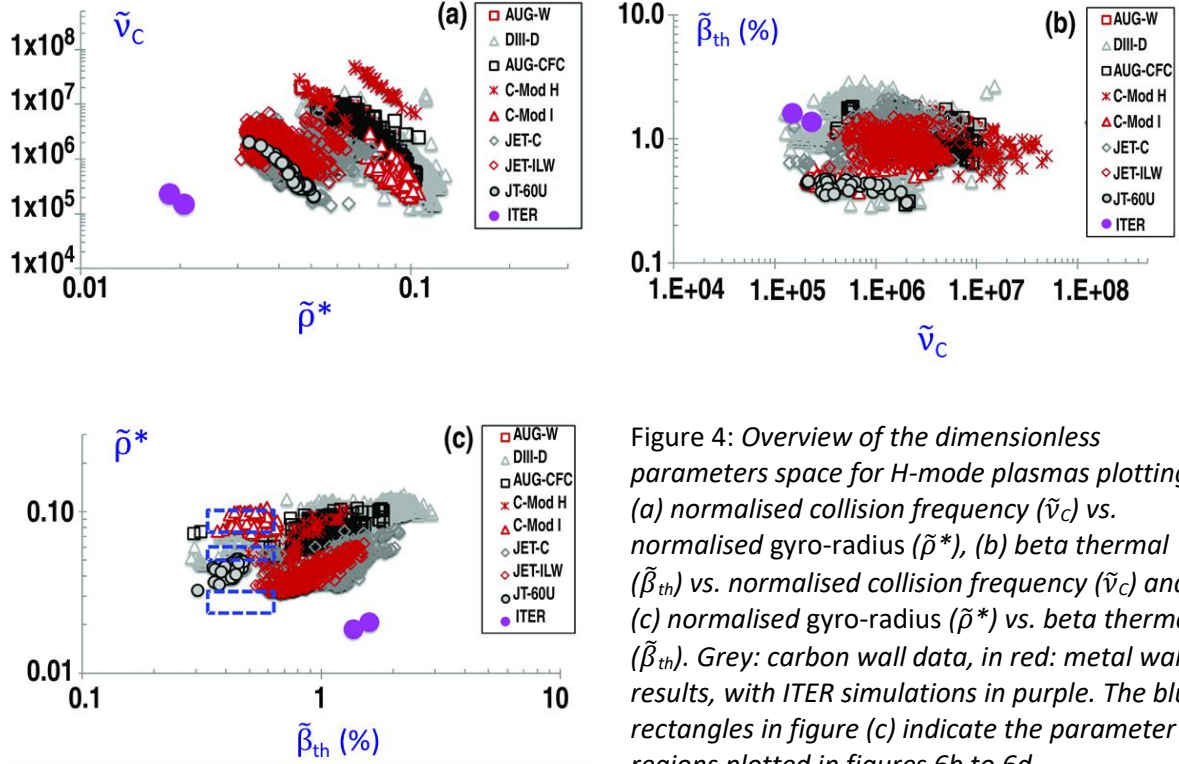the scaling used for projections to ITER.

Figure 4: *Overview of the dimensionless parameters space for H-mode plasmas plotting (a) normalised collision frequency ($\tilde{\nu}_C$) vs. normalised gyro-radius ($\tilde{\rho}*$), (b) beta thermal ($\tilde{\beta}_{th}$) vs. normalised collision frequency ($\tilde{\nu}_C$) and (c) normalised gyro-radius ($\tilde{\rho}*$) vs. beta thermal ($\tilde{\beta}_{th}$). Grey: carbon wall data, in red: metal wall results, with ITER simulations in purple. The blue rectangles in figure (c) indicate the parameter regions plotted in figures 6b to 6d.*

Dimensionless parameters for the database are shown in Figure 4. The definitions used are

[26]:

$$\rho^* \sim \tilde{\rho}^* = \sqrt{W_{th}/n_e V}/(a B_0) \tag{2}$$

where $\tilde{\rho}*$ is a proxy for the normalised gyro-radius,

$$\nu_C \sim \tilde{\nu}_C = \left(n_e^3 V^2/W_{th}^2\right)\sqrt{R_{geo}^5/a^3} \tag{3}$$

where $\tilde{\nu}_C$ is a proxy for the normalised collision frequency, and

$$\beta_{th} \sim \tilde{\beta}_{th} = W_{th}/(V B_0^2) \tag{4}$$

for the ratio of thermal kinetic to magnetic pressure (where, together with parameters defined earlier, V is the plasma volume (in m^{-3}) and W_{th} the thermal stored energy (in MJ). Here $\tilde{\beta}_{th}$ (given in % in this paper) is a proxy for the plasma β, being the ratio of plasma pressure to the magnetic pressure and is distinct from β_N which describes the ideal MHD stability limit of a free-boundary plasma in the absence of a wall. In Figure 4, the data at q_{95} ~ 3 are plotted.

The dimensionless parameter definitions in Eq (2) to (4) are not identical to the standard definitions as given in Table 3 in [27]. The expression used for normalised gyro-radius, beta and collision frequency are good proxies for the average values of ρ^*, ν_C and β_{th}. These definitions are particularly suited for analyses using 0-D database vales for W_{th}, n_e, V, a, B_0 and R_{geo}. Since the safety factor is held ~fixed in our database, it is not possible to distinguish between the scaling of heat transport with different normalizations of the collision frequency, such as the collision frequency normalized to the thermal transit time (ν_C) or the collision frequency normalized to the bounce frequency (ν^*). The quantity ν^* is only important theoretically in that it distinguishes where trapped particles play a role. The quantity ν_C however, maintains orthogonality of the dimensionless parameters used. Hence, our results will be given in terms of ν_C, as in other published work from the IOS-TG, e.g. [26].

Concerning $\tilde{\rho}^*$ and $\tilde{\nu}_C$, the data from each device show that they are anti-correlated (negative slope in figure 4a), while the overall cross-machine dataset shows a positive correlation, certainly for the minimum $\tilde{\nu}_C$ versus maximum $\tilde{\rho}^*$. The correlation between $\tilde{\beta}_{th}$ and $\tilde{\nu}_C$ is very weak as shown in Figure 4b, while $\tilde{\rho}^*$ increases with $\tilde{\beta}_{th}$ for each device, in-line with the definitions given in Eq (2) and Eq (4). Compared to the deuterium plasmas in the database, the ITER values for $\tilde{\rho}^*$ are significantly outside the existing dataset (> 2 times smaller in ITER). The single-facility trends of anti-correlated $\tilde{\rho}^*$ and $\tilde{\nu}_C$ are likely also to be observed in ITER, while extrapolation of the overall trend is consistent with the expectation that points close to the ITER target may be accessible. However, achieving the required $H_{98y2} = 1$ in ITER depends on scaling of energy confinement towards low $\tilde{\nu}_C$

and most importantly the extrapolation to lower $\tilde{\rho}*$. This motivates understanding whether these trends reflect a true physical scaling as reviewed in [27].

Several publications [27,28, 29, 30] show that if energy transport is dominated by plasma physics, the normalized thermal energy confinement time may be expressed as:

$$\omega_c \tau_{th} \propto B\tau_{th} \propto f(\rho^*, \beta_{th}, \nu_C, q, \varepsilon, \delta, \kappa, T_i/T_e, ...) \qquad (5)$$

with ω_c the cyclotron frequency and τ_{th} the thermal energy confinement time, not including contributions from fast particles, q is the safety factor, $\varepsilon = a/R_{geo}$ is the inverse plasma aspect ratio, κ is the elongation of the plasma cross-section (ratio of height to width), δ is the triangularity at the plasma separatrix, and T_i and T_e are, respectively, ion and electron temperature. A generalised expression of the normalised confinement with the main dimensionless parameters has the following power-law form:

$$B\tau_{th} \propto \rho^{*\alpha_\rho} \beta_{th}^{\alpha_\beta} \nu_C^{\alpha_\nu} q_{95}^{\alpha_q} \varepsilon^{\alpha_\varepsilon} \kappa^{\alpha_\kappa} \qquad (6)$$

A power-law form for the dependence of $B\tau_{th}$ on the dimensionless parameters is not required by dimensional analysis but is convenient in comparisons with the traditional power-law scaling applied to the engineering variables such as used in Eq (1). Having collected stationary H-mode data for a restricted range of the dimensionless variable q_{95} = 2.7 - 3.3, the amount of data collected is such that trends of the normalized thermal energy confinement time can be studied, while restricting the other dimensionless parameters to a narrow range of the experimentally observed variation, "slicing" the database in dimensionless parameter space.
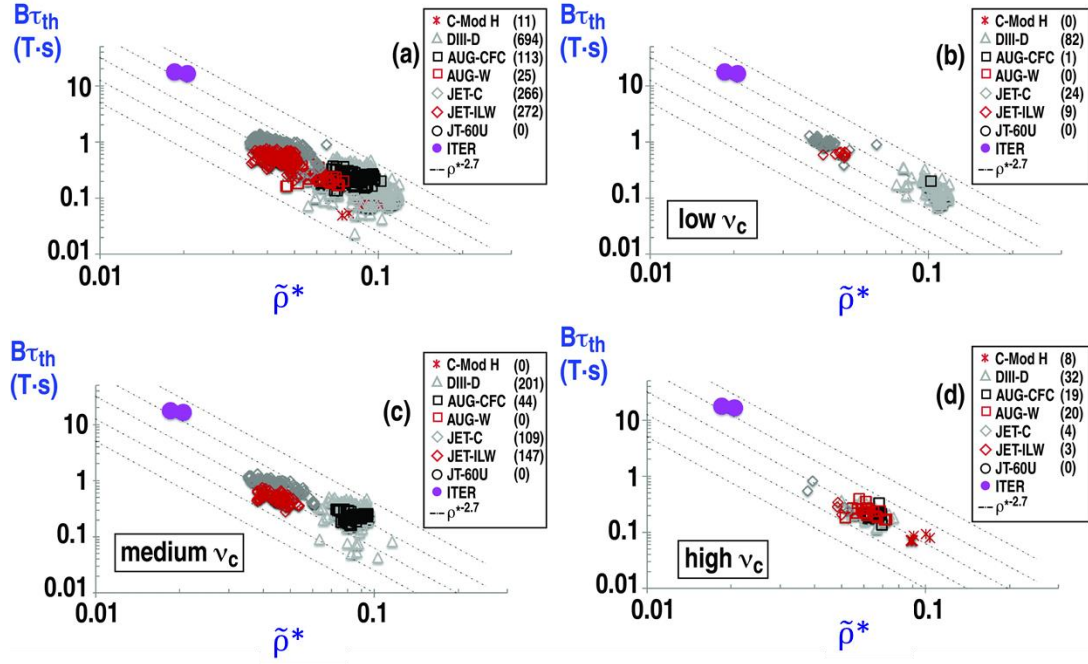
Figure 5: *Dimensionless parameter space of carbon wall and metal wall devices; $B\tau_{th}$ vs gyro-radius. Grey: carbon wall data, red: metal wall results, with ITER simulations in purple. The number of points from each device is given in the legend. The normalised beta (β_N) is restricted to 1.5 - 2.1 for all plots shown. (a) the full range of plasma collision frequency is plotted. For Figures (b) to (d) restricted ranges for collision frequency are plotted (but not applied to ITER simulations): (b) the values for $B\tau_{th}$ are plotted for $\tilde{\nu}_C$ in the range 1 x 10⁵ to 6 x 10⁵ (including ITER range of collision frequencies), (c) for $\tilde{\nu}_C$ in the range 1 x 10⁶ to 2 x 10⁶, and (d) for $\tilde{\nu}_C$ in the range 5 x 10⁶ to 1.5 x 10⁷. Lines for $B\tau_{th} \propto \tilde{\rho}^{*-2.7}$ are plotted for comparison.*

This is first done for the dependence of $B\tau_{th}$ on $\tilde{\rho}^*$, restricting range of β_N = 1.5 to 2.1 from a full range of β_N of 0.5 to 3.8 in the dataset and is equivalent to restricting $\tilde{\beta}_{th}$ from 0.7 % to 1.3 %. Hence, the I-mode data from C-Mod and the H-mode data from JT-60U are not shown as they all have lower β_N. In Figure 5a the full range of $\tilde{\nu}_C$ = 1.3 x 10⁵ to 1.4 x 10⁸ is plotted giving, 1383 data points with data for the measured quantities used to compute the dimensionless parameters. The trend is clear in Figure 5a of increasing $B\tau_{th}$ at lower $\tilde{\rho}^*$, but this is mainly a result from the definition of $\tilde{\rho}^*$ as given in Eq (3), with an inverse B dependence. However, from Figure 5a it is difficult to determine if the dependence is gyro-Bohm, like as for drift wave driven transport [31], with $B\tau_{th} \propto \rho^{*-3}$, or more Bohm-like [32, 33], with $B\tau_{th} \propto \rho^{*-2}$. Trend lines for $B\tau_{th} \propto \tilde{\rho}^{*-2.7}$ are also plotted in Figure 5, to show comparison of experimental results with the $\tilde{\rho}^*$

dependence of the IPB98(y,2) scaling in dimensionless form (Eq (6)). In Figure 5b, the data shown maintains the restriction on β_N = 1.5 to 2.1 but also restricts $\tilde{\nu}_C$ to 1 x 10⁵ to 6 x 10⁵ (low $\tilde{\nu}_C$ values in the database, 118 data points). In Figure 5c, the data are plotted for $\tilde{\nu}_C$ to 1 x 10⁶ to 2 x 10⁶ (medium $\tilde{\nu}_C$ values in the database, 501 data points). In Figure 5d, the data are plotted for $\tilde{\nu}_C$ to 5 x 10⁶ to 1.5 x 10⁷ (high $\tilde{\nu}_C$ values in the database, 86 data points). The data (slope) show a tendency to more Bohm-like scaling at higher collision frequencies, while at the lowest $\tilde{\nu}_C$ values a scaling more consistent with $B\tau_{th} \propto \tilde{\rho}^{*-2.5\ to-3}$ (close to Gyro-Bohm) is found.

Next, the dependence of the plasma collision frequency is studied, restricting β_N and $\tilde{\rho}^*$. In Figure 6, the dependence of Bτ_{th} on $\tilde{\nu}_C$ is plotted for a restricted range of β_N = 1.5 to 2.1 In Figure 6a, the full range of $\tilde{\rho}^*$ = 0.019 to 0.128 is plotted giving, again, 1383 data points. From the "cloud" of points given in Figure 6a, it would be difficult to determine the dependence of Bτ_{th} on collision frequency. Figure 6b shows the data maintaining the restriction on β_N = 1.5 to 2.1, but also restricting $\tilde{\rho}^*$ to 0.04 ± 0.004 (low $\tilde{\rho}^*$ values in the database, 215 data points, all from JET). The data at the beta values of ITER and low $\tilde{\rho}^*$ show an increase of Bτ_{th} at lower $\tilde{\nu}_C$ values, hence trend lines with dependence of B$\tau_{th} \propto \tilde{\nu}_C^{-0.2}$ are also plotted in Figure 6. In Figure 6c, the data are plotted for $\tilde{\rho}^*$ to 0.075 ± 0.0075 (medium $\tilde{\rho}^*$ values in the database, 386 data points, mainly from AUG and DIII-D). In Figure 6d, the data are plotted for $\tilde{\rho}^*$ to 0.1 to 0.15 (high $\tilde{\rho}^*$ values in the database, 76 data points). The data at medium and highest $\tilde{\rho}^*$ values in the database show a less clear trend of achieving higher Bτ_{th} values at lower collision frequency. For the highest $\tilde{\rho}^*$ values, no clear trend is observed, more consistent with $B\tau_{th} \propto \tilde{\nu}_C^0$.

In Figure 6, the ITER simulation points are included in plots (b) to (d) to indicate their location relative to the x-axes and the data available, although the ITER simulations are at lower $\tilde{\rho}^*$ values than used in the data selection of the plots. This comparison shows in Figure 6d that there are only $\tilde{\nu}_C$ data matching ITER at the highest values of $\tilde{\rho}^*$ in the dataset. They would imply an extrapolation of

these results to ITER in $\tilde{\rho}*$ by an order of magnitude and three orders of magnitude in Bτ_{th} for the
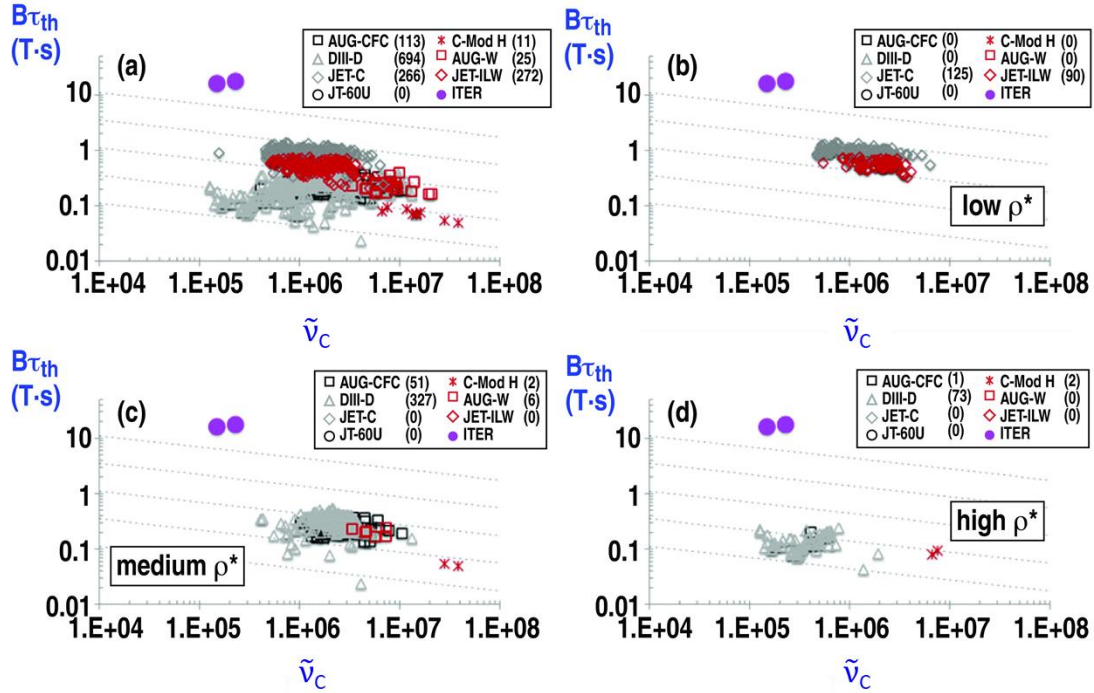
IPB98(y,2) scaling expression in dimensionless form.

Figure 6: *Dimensionless parameter space of carbon wall and metal wall devices; Bτ_{th} vs collision frequency. Grey: carbon wall data, red: metal wall results, with ITER simulations in purple. The number of points from each device is given in the legend. The normalised beta (β_N) is restricted to 1.5 - 2.1 for all plots shown. (a) the full range of normalised gyro-radius is plotted. For Figures (b) to (d) restricted ranges for $\tilde{\rho}*$ are plotted (but not applied to ITER simulations): (b) the values for Bτ_{th} are plotted for $\tilde{\rho}*$ in the range 0.036-0.044 (lowest values in the database), (c) for $\tilde{\rho}*$ in the range 0.0675 - 0.0825, (d) for $\tilde{\rho}*$ in the range 0.1 to 0.15 (highest values in the dataset. Lines for $B\tau_{th} \propto \tilde{v}_C^{-0.2}$ are plotted for comparison.*

Finally, the dependence of Bτ_{th} on beta is studied as shown in Figure 7, where dependence of

Bτ_{th} with $\tilde{\beta}_{th}$ is given for a restricted range of $\tilde{\rho}*$ in the range 0.036 - 0.044 (lowest values in the

dataset, from JET and JT-60U). In Figure 7a, Bτ_{th} versus $\tilde{\beta}_{th}$ is plotted for the full range of $\tilde{v}_C = 1.3 \times$

10^5 to 1.4×10^8 giving 397 data points. Already over the full range of collision frequency these data

show no degradation of Bτ_{th} with $\tilde{\beta}_{th.}$ Trend lines of $B\tau_{th} \propto \tilde{\beta}_{th}^{-0.9}$ are also plotted in Figure 7, clearly

indicating that this trend (as given by the IPB98(y,2) scaling in dimensionless form) is not represented

by the data. Restricting $\tilde{v}_C$ to 1×10^5 to 6×10^5 (low $\tilde{v}_C$ values in the database, 30 data points) is

shown in Figure 7b. In Figure 7c the data are plotted for $\tilde{v}_C$ to 1×10^6 to 2×10^6 (medium $\tilde{v}_C$ values in

the database, 150 data points). In Figure 7d the data are plotted for $\tilde{\nu}_C$ to 3 x 10⁶ to 1.5 x 10⁷ (high $\tilde{\nu}_C$

values in the database, 52 data points). The data maintain the trend that Bτ$_{th}$ shows no degradation

with $\tilde{\beta}_{th}$, if anything the dependence at the highest collision frequency becomes slightly positive with

beta. In Figure 7a, also data at the higher values for normalised gyro-radius in the range 0.1 to 0.15

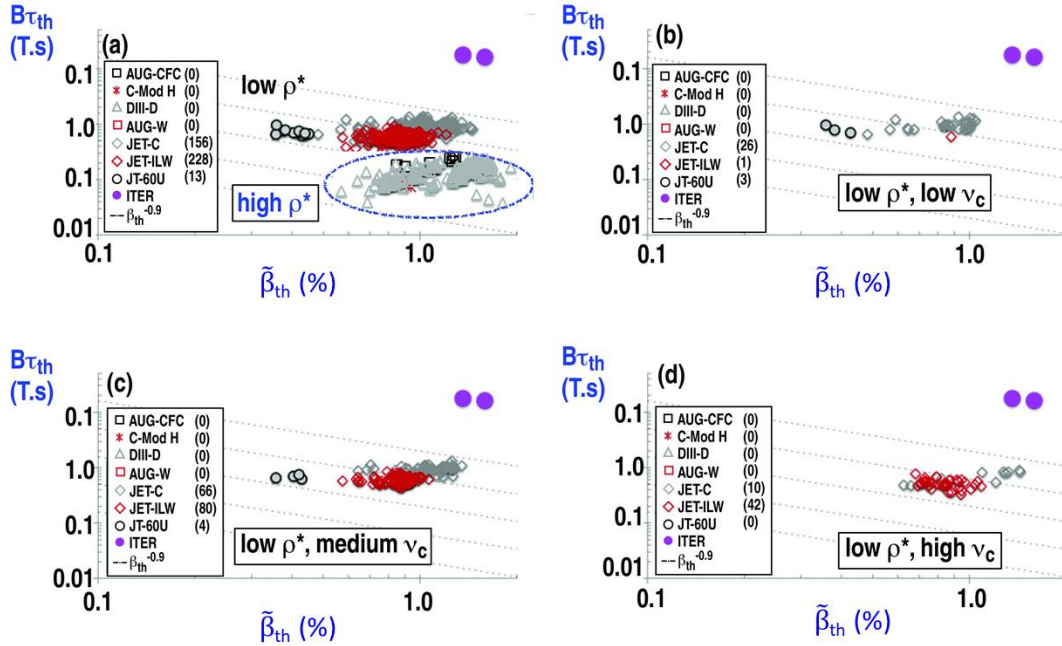are plotted (enclosed by the blue-dotted line), these data also show a similar trend of Bτ$_{th}$ with beta.

Figure 7: *Dimensionless parameter space of carbon wall and metal wall devices; Bτ$_{th}$ vs beta thermal (in %). Grey: carbon wall data, red: metal wall results, with ITER simulations in purple. The number of points from each device is given in the legend. The normalised gyro-radius $\tilde{\rho}*$ is in the range 0.036 - 0.044 (lowest values in the dataset) for all plots shown. In (a) the full range of normalised collision frequency is plotted. Also indicated (enclosed by the blue-dotted line) are data for normalised gyro-radius in the range 0.1 - 0.15 that show the same trend of Bτ$_{th}$ with $\tilde{\beta}_{th}$. In (b) data with collision frequency from 1 x 10⁵ to 6 x 10⁵ are plotted. In (c) data with collision frequency from 1 x 10⁶ to 2 x 10⁶ are plotted. For (d) data with collision frequency in the range 3 x 10⁶ to 1.5 x 10⁷. Lines for $B\tau_{th} \propto \tilde{\beta}_{th}^{-0.9}$ are plotted for comparison.*

5. Comparisons with energy confinement scaling laws

Without restricting the dimensionless parameter space, the data can be compared to scaling

laws for energy confinement. Sufficient data are available (2504 entries, with data for dimensionless

variables), so that the data from devices with a carbon wall (1686 entries from AUG, DIII-D, JET and

JT-60U) can be plotted separately from the data proved from devices with a high-Z metal wall (818

entries from AUG, C-Mod and JET).

The IPB98(y,2) scaling given in Eq (1) has dimensionless form [27, Eq (4.6)]:

$$B\tau_{th,IPB98} \propto \rho^{*-2.69}\ \beta_{th}^{-0.9}\ \nu_C^{0.08}\ q_{95}^{-3.0}\ \varepsilon^{0.73}\ \kappa^{3.29}\ R_{geo}^{-0.01} \tag{7}$$

here, the negligible $R_{geo}^{-0.01}$ dependence depicts the residual non-conformance of the IPB98(y,2)

scaling expression with the dimensionless constraint. Using the IPB98(y,2) scaling in dimensionless

form, the entries of the database presented in this paper are shown in Figure 8. The data have an

overall RMS error of 190 % (combining all devices, the ITER simulation results are not included in

these RMS analyses), indicating that the underlying transport physics processes are not well captured

by the scaling expression. The carbon wall data have an RMS error of 200 % and the data from high-Z

wall devices have an RMS error of 170 %, showing not much difference. The strong scaling with

elongation of the IPB98(y,2) scaling in dimensionless form warrants the question if the plots shown in

Figures 5 to 7 should have restricted the range of κ. However, restricting κ to a range 1.6 - 2.0 (ITER

value of 1.8 ± 10 %) only removes 5 % of the data, including all the data from JT-60U, without

changing the trends shown.

A pure gyro-Bohm and electrostatic scaling (called DS03) as suggested in [34, Eq (13)] with

expression:

$$B\tau_{th,DS03} \propto \rho^{*-3}\ \beta_{th}^{0}\ \nu_C^{-0.14}\ q_{95}^{-1.84}\ \varepsilon^{-1.1}\ \kappa^{2.29}\ R_{geo}^{0.01} \tag{8}$$

provides a better correlation with the data, as shown in Figure 8c (carbon wall data) and Figure 8d

(high-Z metal wall data), with RMS error of 92 % for all the data. The carbon wall data have an RMS

error of 73 % and the data from high-Z wall devices have an RMS error of 122 %. The data from high-

Z walls follow the DS03 scaling well, apart from the data at the largest values of Bτ$_{th}$. These are

provided by JET operating at high plasma current (I$_p$ > 2.5MA) and field (B$_0$ > 2.5T), a parameter space

that requires further optimisation towards lower gas fuelling rates whilst avoiding tungsten

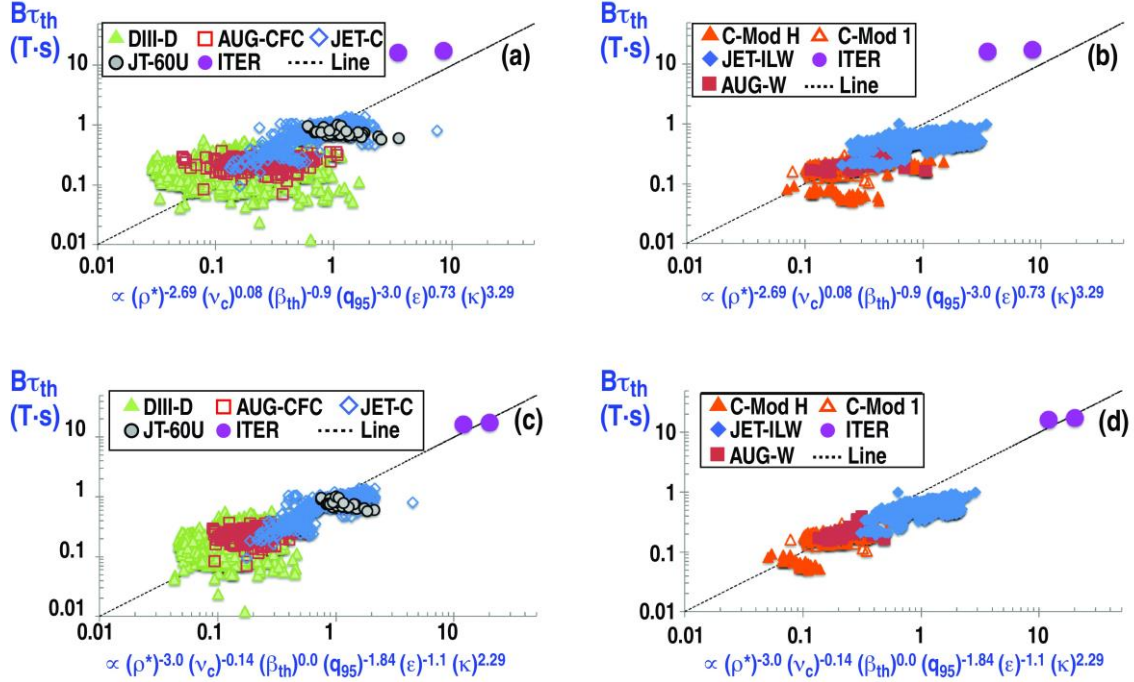accumulation, as outlined in [24].

Figure 8: Comparison of Bτth and dimensionless scaling expressions. Left: Carbon wall data. Right: Data from high-Z metal wall devices. Each device is colour coded, ITER simulations are in purple. (a) and (b) IPB98(y,2) scaling, and (c) and (d) gyro-Bohm, electrostatic turbulence scaling (DS03).

It is common practice to plot normalised confinement values (such as H_{98y2}) versus $\tilde{\rho}^*$, $\tilde{\nu}_C$ or $\tilde{\beta}_{th}$ (or β_N) without restricting the domain of the other dimensionless parameters. In Figure 9, H_{98y2} is plotted versus $\tilde{\nu}_C$, showing that the maximum H_{98y2} that can be obtained for a given collision frequency increases with decreasing collision frequency. Similar trends with collision frequency are observed in the ITPA-IOS TG database for advanced inductive discharges [26]. It is remarkable that the maximum values for H_{98y2} obtained as a function of collision frequency are similar for a range of experiments as shown in Figure 9. No difference in normalised confinement is observed between carbon wall and metal wall discharges at high collision frequency (> 5 x 10⁶) and the trends towards lower collision frequency show a similar rate of increase in confinement enhancement, H_{98y2}. However, data from experiments with carbon walls have routinely achieved lower collision frequencies compared to experimental results in devices with metal walls: Carbon wall results continue to increase in maximum obtainable H_{98y2} factors at lower collision frequency. The standard H-mode scaling does not seem to have the correct collision frequency dependence, however as seen

from Figure 4, the collision frequency is correlated with the normalised gyro-radius, hence other factors for trends in H_{98y2} will play a role. Overview plots as shown in Figure 9 are useful for illustrating comparisons of the operational space between several devices, using (dimensionless) normalisation parameters, but have limited value in presenting plasma confinement trends as they may merely depict deficiencies in the scaling law used.
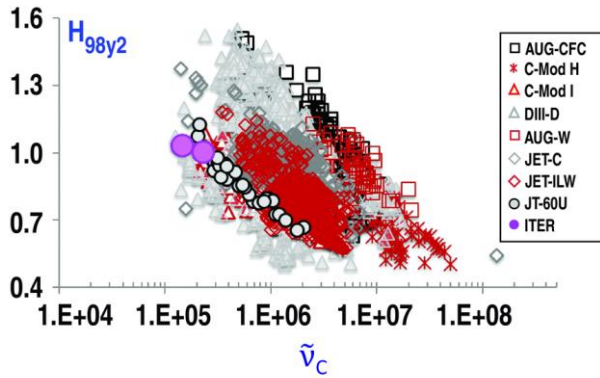

Figure 9: *Comparison of carbon wall and metal wall results; normalised confinement (H_{98y2}) vs. normalised collision frequency $\tilde{\nu}_C$. Grey: carbon wall data, red: metal wall results, with ITER simulations in purple.*

Scaling laws with engineering variables have been used to compare results of experiments in existing devices and to predict the energy confinement of future devices. The most commonly used IPB98(y,2), as given in Eq (1) was derived using data from 11 devices with a large range in parameters [35, Table II], such as I_p (0.14 MA to 5.1 MA), P_{loss} (0.18 MW to 18 MW), R_{geo} (1.3 m to 2.9 m), q_{95} (1.9 to 11.1), n_e (1.1 x 10^{19} m^{-3} to 43 x 10^{19} m^{-3}) and normalised beta (0.5 to 3.5). The main differences with the database presented here is the restriction for q_{95} from 2.7 to 3.3, the data being provided only from five (ITER-like) devices and the larger range for P_{loss} (0.5 MW to 30 MW). Another difference is that the original database for IPB98(y,2) allowed points with $(-0.05 \leq (dW_{th}/dt)/P_{loss} \leq 0.35)$, with no criteria on achieving stationarity for five confinement times as applied for the data at q_{95} ~ 3, giving $(-0.05 \leq (dW_{th}/dt)/P_{loss} \leq 0.15)$. The analyses of the original database, summarised in [10], insured that the scaling expression found (with an RMS

error of 15.6 %) was a valid representation of the data, and that correlations among the data were
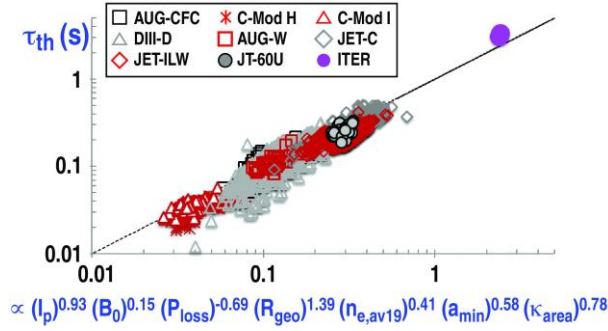
appropriately dealt with.

Figure 10: Grey: carbon wall data, red: metal wall results, with ITER simulations in purple. Plot of the scaled thermal energy confinement, versus measured τ_{th} for the IPB98(y,2) scaling as given in Eq (1).

In Figure 10, the computed τ_{th} for the data at q$_{95}$ ~ 3 is compared with the IPB98(y,2) scaling

prediction. Plotted on a log-log scale, the data for each device seem to follow the scaling with a

normalised RMS error for all the data of 28 %, and an average value for H$_{98y2}$ of 0.91. This RMS is

substantially smaller compared to the RMS error obtained from the dimensionless scaling regressions

(190 %). This is due to the high exponents of the ρ*, q$_{95}$ and κ dependencies in the dimensionless

scaling, amplifying any discrepancy with the scaling expression, or that additional dimensionless

parameters need to be considered. However, the RMS value is larger than the RMS value (15.6 %) of

the original dataset for the IPB98(y,2) scaling. As shown in Table IV at the end of this section, the

RMS error of the data from devices with a carbon wall is 25 %, with H$_{98y2}$ ~ 0.97, while the RMS error

of data from high-Z metal wall devices is 34 % with H$_{98y2}$ ~ 0.80. The original data set for IPB98(y,2)

scaling contained mainly results from carbon wall devices. Moreover, the data for q$_{95}$ ~ 3 certainly lie

at the extreme range for q$_{95}$ of the original data. It is possible that the single power law model

assumed for the IPB98(y,2) scaling regression breaks down, or at least acquires some curvature, near

q$_{95}$ = 3.

	τ_{th}	I_p	B_0	P_{loss}	R_{geo}	a	κ_a	n_e
τ_{th}	1	0.76	0.01	0.51	0.85	0.84	0.13	-0.27
I_p	0.76	1	0.46	0.86	0.75	0.75	-0.06	-0.09
B_0	0.01	0.46	1	0.25	-0.10	-0.15	-0.35	0.56
P_{loss}	0.51	0.86	0.25	1	0.77	0.75	0.00	-0.15
R_{geo}	0.85	0.75	-0.10	0.77	1	0.99	0.06	-0.49
a	0.84	0.75	-0.15	0.75	0.99	1	0.02	-0.53
κ_a	0.13	-0.06	-0.35	0.00	0.06	0.02	1	0.01
n_e	-0.27	-0.09	0.56	-0.15	-0.49	-0.53	0.01	1

Table III: The correlation matrix of the logarithm of the variables used in the IPB98(y,2) scaling law given in Eq (1).
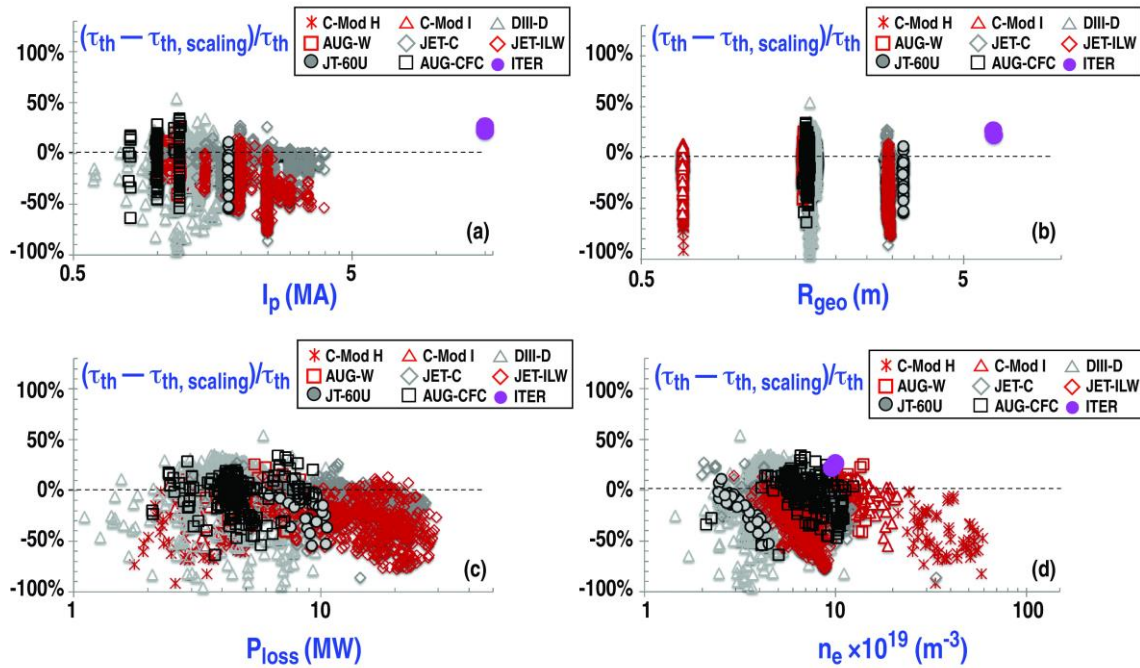

Figure 11: The residuals for the IPB98(y,2) scaling plotted as a function of the four main variables: (a) I_p, (b) R_{geo}, (c) P_{loss} and (d) n_e. Grey: carbon wall data, red: metal wall results.

Some of the variables used in IPB98(y,2)) scaling expression have a very high correlation in the database at q₉₅ ~ 3 as shown in Table III; minor radius and R₉ₑₒ have Pearson correlation R = 0.99, as the devices contributing to the database at q₉₅~ 3 have very similar aspect ratio (R_{geo}/a). Other parameters, such as B₀, κₐ and nₑ, have no or a low correlation with τₜₕ, in the database presented in

this paper. Even though the fit parameters used for the IPB98(y,2) are justified for the data in the original database of the mid-1990's, for the data collected on the ITER baseline for the devices listed in table II, the IPB98(y,2) scaling represents an "overfit" (using too many variables) for the data at q_{95} ~ 3. The residuals for the IPB98(y,2) scaling, defined as the relative variation of measured minus scaling confinement time $(\tau_{th} - \tau_{th,IPB98})/\tau_{th}$, for the four main variables I_p, P_{loss}, R_{geo} and n_e are plotted in Figure 11. Clear trends in these residuals are observed.

For the IPB98(y,2) scaling, the residual dependence of the confinement time with plasma density is most pronounced (Figure 11d). The data trend from a single device show typically a weaker density dependence, as the confinement using IPB98(y,2) scaling is over-predicted at higher densities. This is particularity true for devices with a high-Z metal wall; the data from the high-Z metal wall devices have no dependence of the confinement time on plasma density.
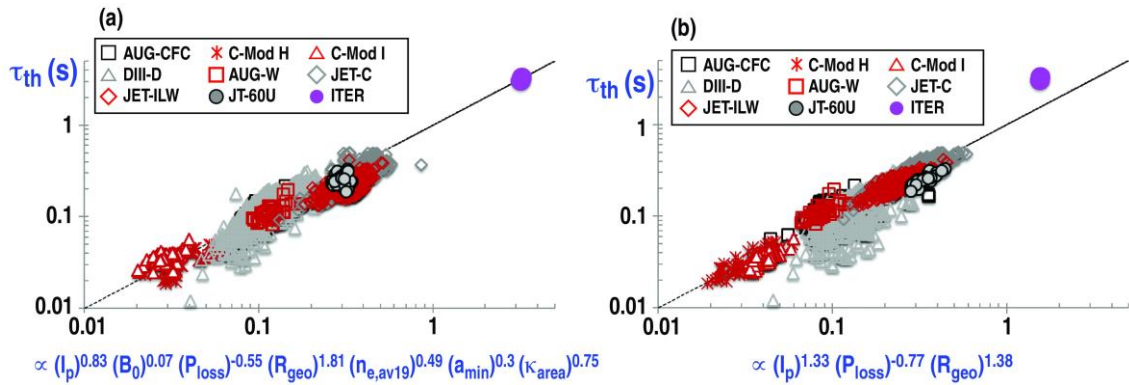

Figure 12: Grey: carbon wall data, red: metal wall results, with ITER simulations in purple. (a) plot of the scaled thermal energy confinement, versus measured τ$_{th}$ for the DS03 scaling as given in Eq (9). (b) plot of the scaled thermal energy confinement, versus measured τ$_{th}$ for scaling with three variables only, as given in Eq (10).

A pure gyro-Bohm and electrostatic scaling (DS03), which gives a better representation of the data compared to IPB98(y,2) in dimensionless form as shown in section 5 (Figure 8), has the following expression using engineering parameters [34, Eq (12)], using ion mass A equal to 2:

$$\tau_{DS03}[s] = 0.028\, P_{loss}^{-0.55}\, B_0^{0.07}\, I_p^{0.83}\, \kappa_a^{0.75}\, n_e^{0.49}\, a^{0.3}\, R_{geo}^{1.81}\, 2^{0.14} \qquad (9)$$

The thermal energy confinement times computed using this scaling expression are given in Figure 12a and have an RMS error of 34 % compared to τ_{th} provided, as shown in Table IV (with an RMS error of 26 % for carbon wall data, and 46 % for data from high-Z metal wall devices). Although not shown here, the residuals for the four main parameters I$_p$, P$_{loss}$, R$_{geo}$ and n$_e$ also show residual trends for the DS03 scaling.

Reasonable fits to the data in the database can be obtained using only three fit parameters (I$_p$, P$_{loss}$, and major radius, R$_{geo}$). The scaling of the thermal energy confinement obtained is:

$$\tau_{3\_parameters} \, [s] = 0.16 \, P_{loss}^{-0.77} \, I_p^{1.33} \, R_{geo}^{1.38} \tag{10}$$

The use of I$_p$, P$_{loss}$, and R$_{geo}$ is justified as these parameters have the highest correlation with the observed thermal confinement time, while containing over 90 % of the information in the scaling. The regression using I$_p$, P$_{loss}$, and R$_{geo}$ has an RMS error of 30 % and is shown in Figure 12b. This reduced parameter scaling law is based on data from all devices, with carbon walls and high-Z metal walls, including I-mode data from C-Mod and has no residual scaling with plasma density. However individual devices show some separation compared to the scaling, especially the thermal confinement from DIII-D is overestimated. The reduced parameters scaling expression presented in Eq (10) should not be used as a valid scaling expression for H-mode confinement at q$_{95}$ ~ 3 (nor is Eq (10) dimensionally correct) but should be seen as an exercise showing the main scaling parameters.

	Expression	Figure	All		C wall		Metal wall	
			<H>	RMS	<H>	RMS	<H>	RMS
IPB98(y,2) scaling	Eq (1)	Fig. 10	0.91	28 %	0.97	25 %	0.80	34 %
DS03 scaling	Eq (9)	Fig. 12a	1.12	34 %	1.22	26 %	0.94	46 %
3-parameters only	Eq (10)	Fig, 12b	1	30 %	1.02	35 %	0.96	15 %

Table IV: Overview of normalised confinement factor and RMS error for two scaling expressions and an expression using the three main scaling parameters in the dataset.

6. Plasma confinement trends with beta and plasma density

Despite the shortcomings of the IPB98(y,2) scaling, it continues to be regarded as the standard confinement scaling expression. Hence, it will be used in the remainder of this paper to present the analyses of the database at q$_{95}$ ~ 3.

The dimensionless analyses given in the previous sections, indicates that the scaling with beta for IPB98(y,2) is too pessimistic. The scaling with loss power ($P_{loss}^{-0.69}$) is not in agreement with observations of no change in normalised confinement time with input power or beta in dedicated experiments in DIII-D [27] and JET [36, 37]. The database shows that the maximum achievable H$_{98y2}$ increases with β_N (see Figure 13). This trend with β_N is also observed in the advanced inductive discharges [26]. Stationary discharges at q$_{95}$ ~ 3 and H$_{98y2}$ ≥ 1.0 are obtained for a wide range of β_N in experiments with carbon walls, using pre-dominantly co-current NBI heating (AUG, DIII-D and JET). At high β_N > 2 discharges at q$_{95}$ ~ 3 in DIII-D and AUG with a carbon wall reach H$_{98y2}$ = 1.4 - 1.5, similar to hybrid regimes at higher q$_{95}$ ~ 4. The increase in H$_{98y2}$ with beta is most apparent for high-Z metal wall devices. In H-modes obtained with metal walls in AUG, C-Mod and JET, the confinement is significantly reduced (H$_{98y2}$ ~ 0.8 - 0.9) at β_N < 1.8 with only the best discharges obtaining H$_{98y2}$ ~ 1 at the ITER beta of β_N = 1.8. ELMy H-mode discharges with high-Z walls and at low input power (and beta) require additional gas dosing to control the tungsten accumulation in the core. The gas dosing increases the ELM frequency, reducing the pedestal pressure and global energy confinement. On the other hand, discharges with a carbon wall can operate at very low ELM frequency (< 5Hz) and no gas dosing maximising the pedestal pressure up to the peeling-ballooning limit even at low plasma beta, resulting in a large operating space as indicated in Figure 13a. With high-Z metal walls, stationary discharges at q$_{95}$ ~ 3 and H$_{98y2}$ ~ 1 are typically only obtained at β_N ~ 2 or higher. The observed reduced confinement at low β_N will affect the entry to burn in ITER, as simulations currently assume H$_{98y2}$ = 1 after transition to H-mode. The exception are I-mode discharges in C-Mod and dominant ICRF heated discharges with the carbon wall at JET (blue open diamonds at β_N < 1.8 in Figure 13a),

they achieve good thermal confinement at low β_N. Both C-Mod and JET achieve these results at low

Greenwald density fraction f_{GW} ~ 0.2 and relatively high plasma inductance values $l_i(3)$ ~ 1 - 1.1.
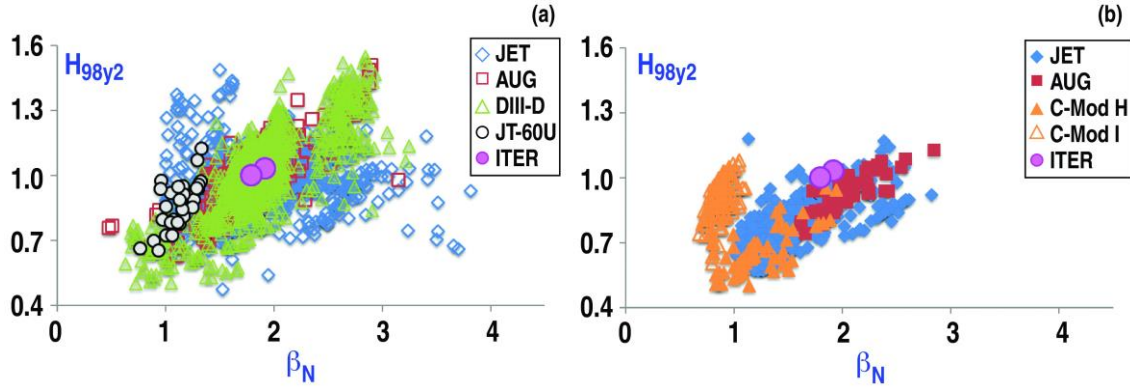

Figure 13: *Comparing devices with a carbon wall (a) and metal wall (b); the normalised H-mode confinement (H$_{98y2}$) as a function of the normalised beta obtained (β_N).*
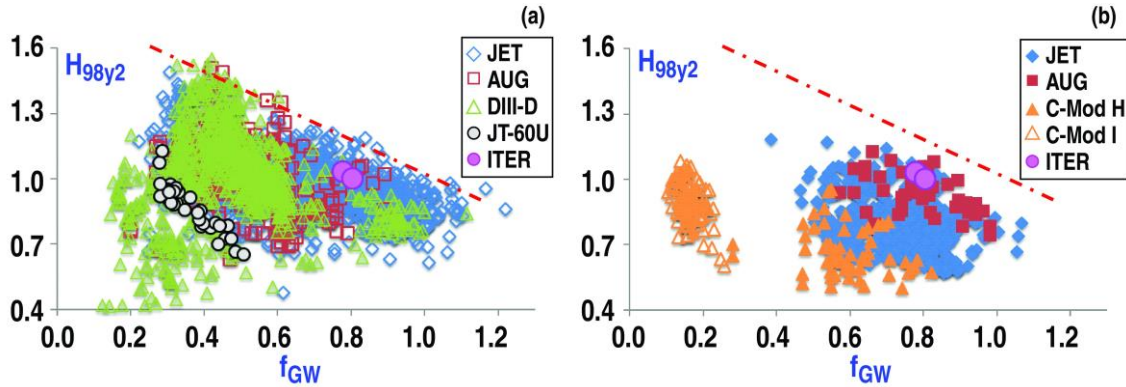

Figure 14: *Comparing devices with a carbon wall (a) and metal wall (b); the normalised H-mode confinement (H$_{98y2}$) as a function of the Greenwald density fraction achieved (f$_{GW}$). The dashed red line denotes an empirical trend line for the maximum H-factor obtained for a given Greenwald fraction for carbon wall devices, which is repeated in figure (b).*

Fuelling studies of stationary H-modes at q$_{95}$ ~ 3 indicate that in some experiments it is not

possible to reach f_{GW} > 0.8 in H-mode. In C-Mod the density is limited to f_{GW} < 0.80 for H$_{98y2}$ > 0.8,

operating in configurations matching the ITER shape. The carbon wall data show a drop in H$_{98y2}$ with

increasing f_{GW}, as do metal wall results as shown in Figure 14. However, for any f_{GW} value, the

maximum H$_{98y2}$ achieved is lower in high-Z metal wall devices as indicated by the dashed red lines in

Figure 14. The ITER requirement of $f_{GW} \sim 0.85$ with $H_{98y2} = 1$ is at the top of the data range available in experiments with metal walls.

In the early stages of the ITER design, the plasma shape was chosen with a triangularity $\delta \sim 0.5$, aimed at maximising the pedestal stored energy and to obtain $H_{98y2} \sim 1$ at high plasma density with $f_{GW} \sim 0.85$. For H-mode discharges that obtain $H_{98y2} > 0.95$, the dataset for carbon wall and metal wall discharges shows indeed an overall increase of f_{GW} attainable with average triangularity as shown in Figure 15, although only a few discharges for JET-ILW are available at the operating point of ITER. The data at $f_{GW} \sim 1$ with the carbon wall at JET were obtained in the so-called mixed type I+II ELM regimes using plasma configurations at high triangularity ($\delta \sim 0.45 - 0.5$) [38], this regime could not be established with the JET-ILW. Some discharges with the tungsten wall at AUG do reach the ITER requirement of good confinement at $\delta \sim 0.35$. C-Mod operates at the ITER triangularity value and at much higher absolute plasma density than other devices (including ITER). However, with the too strong density dependence in the IPB98(y,2) scaling, typical H_{98y2} values for C-Mod are ~ 0.8. Hence, only one H-mode discharge from C-Mod is plotted in Figure 15, together with I-mode discharges from C-Mod at low f_{GW} that do obtain $H_{98y2} > 0.95$. DIII-D has no data at $f_{GW} > 0.6$ for high plasma shaping at $q_{95} \sim 3$. As a result, for triangularity > 0.5 there are no data available at $f_{GW} \sim 0.85$ and $H_{98y2} > 0.95$ from any of the experiments, providing no guidance if ITER could be further optimised by operating at higher triangularity than the baseline separatrix value of $\delta_x \sim 0.5$.
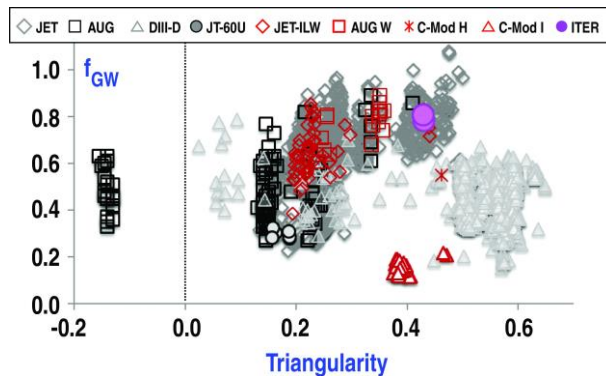

Figure 15: *Comparison of carbon wall and metal wall results; Greenwald density fraction (f_{GW}) vs triangularity $\left(\delta^{upper} + \delta^{lower}\right)/2$ for discharges with $H_{98y2} > 0.95$. Grey: carbon wall data, red: metal wall results, with ITER simulations in purple.*

For AUG with the tungsten wall and JET with the ILW no data are available with gas fuelling rates below 1×10^{21} electrons/s; discharges with lower fuelling rates are not stable as gas fuelling is required to reduce the tungsten influxes and ensuring high enough ELM frequency to prevent tungsten accumulation [19, 24]. C-Mod entries in the database are ELM free or have enhanced D-alpha activity (EDA) without discrete ELMs, requiring no gas dosing to obtain stable discharges with the molybdenum wall. The use of gas fuelling at for high-Z metal wall experiments at JET and AUG typically lowers the pedestal pressure, compared to carbon wall experiments, reducing global energy confinement times. Nevertheless, at fuelling rates in the range 5×10^{21}/s to $> 1 \times 10^{23}$/s the plasma confinement is similar for H-mode operation with carbon walls and metal walls, especially for seeded plasmas in AUG [39]. The database contains only a few discharges with nitrogen seeding from both AUG and JET, not enough to obtain trends compared to non-seeded H-mode plasma results. Inter-machine comparisons of electron fuelling rates in H-modes is complicated by the fact that devices have different pumping speeds and divertor geometries; at the moment it is not clear how these results would scale to ITER. Hence, the reduction of confinement with gas puffing and the roll-over of confinement when approaching the Greenwald density limit would warrant the inclusion of the edge density or recycling flux as additional information to the database, rather than using the line averaged density n_e alone. Kallenbach et al [40] showed that the electron density/neutral hydrogen flux in the scrape-off layer is found to be a key parameter for particle and energy confinement as well as for the radiative losses.

7. Input power and radiation

Obtaining sufficient energy confinement is critical in ITER for entry into H-mode and starting the burn with the installed additional heating power. The total heating power available in ITER (including alpha power, not subtracting core radiation) is nearly two times the power required to enter H-mode (P_{LH}) at baseline operating conditions (f_{GW} ~ 0.85), with the majority of the power provided by alpha

Paper for Nucl. Fusion   **"***Assessment of the Baseline Scenario at q₉₅ ~ 3 for ITER***"**

Final version

heating (P_α ~ 100 MW, P_{aux} ~ 50 MW). For the prediction of P_{LH} the expression given in [41, Eq (2)] is used,

$$P_{LH} [MW] = 0.0488 \, n_e^{0.717} \, B_0^{0.803} \, S^{0.941} \tag{11}$$

where n_e is given in units of 10^{20} m^{-3}, B_0 is given in Tesla and S is the plasma surface area at the separatrix in m^2. However, the measured L- to H-mode threshold power in the experiments may be different compared to the scaling predictions. This is especially the case for discharges in AUG and JET with metal walls where the measured P_{LH} values can be 30 - 40 % below the scaling, depending on plasma density [42, 43].
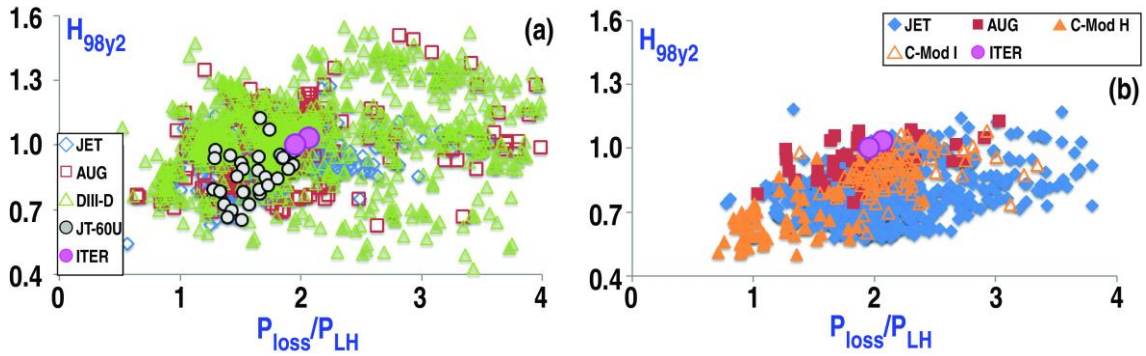

Figure 16: *Comparing devices with a carbon wall (a) and metal wall (b); the normalised H-mode confinement (H₉₈y₂) as a function of loss power (P_loss) normalised to the power required for entry to H-mode (P_LH) [41]. ITER simulations in purple.*

Figure 16 shows the variation of H_{98y2} with P_{loss}/P_{LH}. For discharges with carbon walls, the plasma confinement enhancement factor can be ≥ 1 for any value of $P_{loss}/P_{LH} \geq 1$. At low input power these discharges have low ELM frequency (in JET ~ 1 Hz). In contrast, this is not possible with high-Z metal walls or divertors, as the high-Z impurities (Mo in C-Mod or W in AUG and JET) accumulate in the plasma core, leading to a radiation collapse. These discharges only reach H_{98y2} ~ 1 for P_{loss}/P_{LH} ~ 2, when, with the help of gas dosing, the ELM frequency is high enough (e.g. 15 − 20 Hz in JET) to provide stationary H-mode discharges. Also, data from C-Mod with duration < 5τ_E (more transient)

have confinement similar to stationary discharges with metal walls for P$_{loss}$/P$_{LH}$ in the range 1 to 2.

The requirement for ELM pacing for controlling the plasma radiation during the entry to burn in ITER

is elucidated in [44] and may further reduce the confinement of the plasma in ITER when entering

burn. Burn simulations for ITER [45] do indicate a delicate balance of the assumed impurity radiation

level, confinement properties, plasma density evolution and heating power requirements. Most

simulations apply maximum heating power to initiate the burn, with the density build-up from L-

mode to H-mode not optimised for H-mode access. Optimising the density build-up allows robust
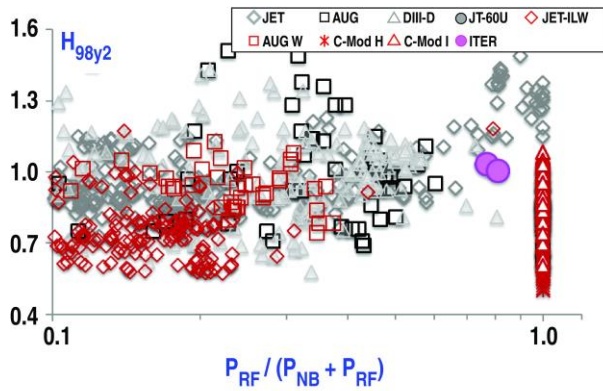
access to Q = 10 with 50 MW of additional heating [46].

Figure 17: Variation of the normalised confinement factor H$_{98y2}$ with fraction of the additional heating supplied by RF heating (ICRH and or ECRH). Grey: carbon wall data, red: metal wall results, with ITER simulations in purple.

Most of the data in the database are provided from experiments with dominant co-NBI,

heating mainly the ions in the core of the plasma, and as a result do not represent the heating

conditions in ITER with dominant electron heating. The data from C-Mod are with pure radio-

frequency (RF) heating. The contribution of the RF heating can be determined using

$P_{RF}/(P_{NB} + P_{RF})$. Although this does not reflect the split between ion and electron heating in the

core, it does represent a measure for changing the heating scheme to more electron heating with

low net torque applied to the plasma. The data with NBI heating alone obtain normalised

confinement, H$_{98y2}$, up to 1.55 in the database. As shown in Figure 17, the data with significant RF

contribution can obtain similar values, and certainly can achieve H$_{98y2}$ ~ 1 in a range of devices over a

range of plasma conditions. This is consistent with experiments in JET [47] showing that no

significant difference in the density and temperature profiles or in the global confinement were found by varying the proportion between ion cyclotron and neutral beam heating. In some cases (such as JET with a carbon wall), pure RF heated discharges obtain very high values for H_{98y2}. Since routine calculations may provide an underestimate of the fast particle population generated by the ICRF minority heating schemes, these discharges would require detailed transport analyses to determine the exact content of the fast particle pressure to determine the correct value for W_{th} for the confinement assessment.

The bulk radiation is not subtracted in the computations of P_{loss}. Also, the total plasma radiation has not been included in the H-mode power threshold scaling [41]. However, the total radiation plays an important role for H-mode dynamics, such as entry into stationary H-modes, as only the power convected through the separatrix contributes to the loss power that keeps the plasma in H-mode. The importance of bulk radiation can be assessed by comparing the radiation normalised to the total input power, i.e. radiation fraction f_{rad}.
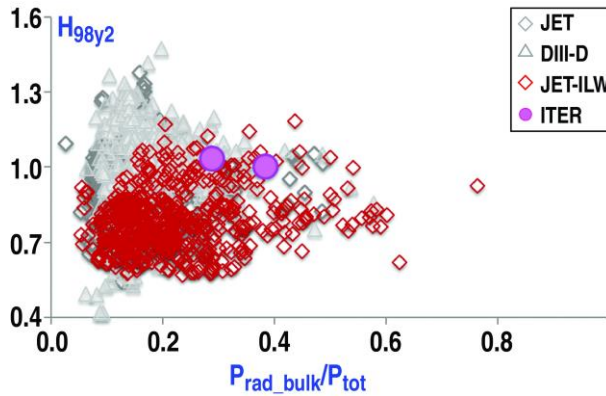

Figure 18: Comparison of carbon wall and metal wall results; normalised confinement (H_{98y2}) vs bulk radiation normalised to total heating power. Grey: carbon wall data, red: metal wall results, with ITER simulations in purple

In the ITER simulations, the total bulk radiation is the sum of bremsstrahlung (P_{brem}), the cyclotron radiation (P_{cycl}) and line radiation (P_{line}) and ranges from 40 MW to 48 MW in the two simulations provided. DIII-D and JET have data for the bulk radiation of H-mode discharges in the database. These values have been obtained by integrating the reconstructed radiation inside the

plasma separatrix, which in some cases may give large uncertainties. Hence, not all experiments have provided values for bulk radiation. The normalised radiation levels, or bulk radiation fraction ($f_{rad} = P_{rad\_bulk}/P_{tot}$) in ITER are in the range 0.29 to 0.39 and are within the data available from the experiments as shown in Figure 18. H_{98y2} does not show a strong variation for P_{rad_bulk}/P_{tot} values between 0.2 and 0.5. In addition, for the total radiation of the plasmas $\left(P_{rad\_bulk} + P_{rad\_SOL\_divertor}\right)$ no difference is observed between carbon wall data and metal wall data for radiation fractions of > 50 %. The best carbon wall discharges (from JET and DIII-D) reach values for H_{98y2} from 1.18 down to 1.0 for radiation fractions increasing from 50 % to 80 %, while AUG (seeded, W wall) discharges obtain $H_{98y2} \sim 1.1$ at radiation fraction > 50 %; like discharges from AUG reported in [39].

Another method to compare radiation values is to normalise to the particle density, as the core radiation is thought to scale with the particle density times the impurity density. The latter is often converted into a scaling with the square of the density, assuming a constant impurity content [48]. In Figure 19, the radiation power, per plasma volume, is plotted versus n_e^2. A satisfactory scaling is found when the radiation is normalised with the entire volume as in the database are not necessarily dominated by edge line radiation with data from devices with both carbon and metal walls. As the discharges in the database are stationary, no strong outliers are observed due to high-Z impurity radiation for devices with metal walls as sometimes observed when entering or terminating H-mode [49]. The experimental values in Figure 19 correspond to radiation cooling qualities within the range of $0.1 \, x \, 10^{-40} \, to \, 1 \, x \, 10^{-40} \, (MW \, m^3)$, as is typical for tokamaks [50, 51] and these values are also found for ramp down studies of H-mode discharges [49]. The ITER simulation results provided here are at the low end of the radiation per volume for the density assumed in the simulations, despite having core tungsten line radiation [52] and an increase in Bremsstrahlung at fusion relevant electron temperatures. The impurity concentrations used in the ITER simulation using CORSICA [17] are $n_{Be}/n_e \sim 1.8 \, x \, 10^{-2}$ and $n_{Ar}/n_e \sim 1.4 \, x \, 10^{-3}$ to give $Z_{eff} \sim 1.7$. Alternatively, with Be and W impurities, $n_{Be}/n_e \sim 2.6 \, x \, 10^{-2}$ was used while n_W/n_e was varied from

$2.6 \, x \, 10^{-7} \, to \, 5.2 \, x \, 10^{-5}$. However, H-mode access would be marginal at $n_W/n_e \sim 1.0 \, x \, 10^{-5}$.

Studies reported in [53] show that the radial convection velocity of tungsten is outward directed for

most of the edge plasma profiles considered for a wide range of ITER operational scenarios using
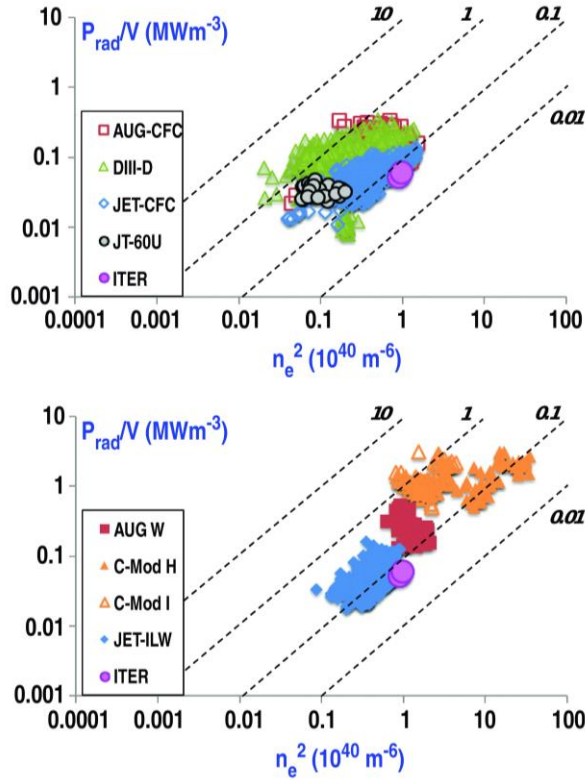
$n_W/n_e \sim 5 \, x \, 10^{-6}$.

Figure 19: Radiative power P_{rad}, normalised to the plasma volume, versus the electron density squared. The dashed lines indicate constant radiation cooling levels in units of 10^{-40} MWm^3. Devices with a carbon wall (top) and metal wall (bottom).

8. Operating space and projected fusion performance

The operating space covered in the dataset at q_{95} ~ 3 is shown in Figure 20, where the achieved β_N in

stationary discharges is plotted against the internal inductance $l_i(3)$. All four machines occupy roughly

the same region of this parameter space and lie within the specified range for the ITER poloidal field

coils for 15 MA operation ($0.6 < l_i(3) < 1.2$). DINA-CH and an advanced transport modelling code,

CRONOS were used [54] for simulations of the 15 MA ELMy H-mode inductive scenario, considering

PF coil current and voltage limits. These studies showed that application of early heating and current

drive is required in ITER to obtain plasma inductance to values of $l_i(3) \sim 0.72 - 0.74$ throughout the fusion burn phase, allowing plasma configurations to be maintained within the PF coil limits. In fact, the PF coil systems in ITER were upgraded from the original designs (before 2009) to allow operation at low $l_i(3)$ (< 0.8) for flattop burn durations of 400 to 500 s [13].
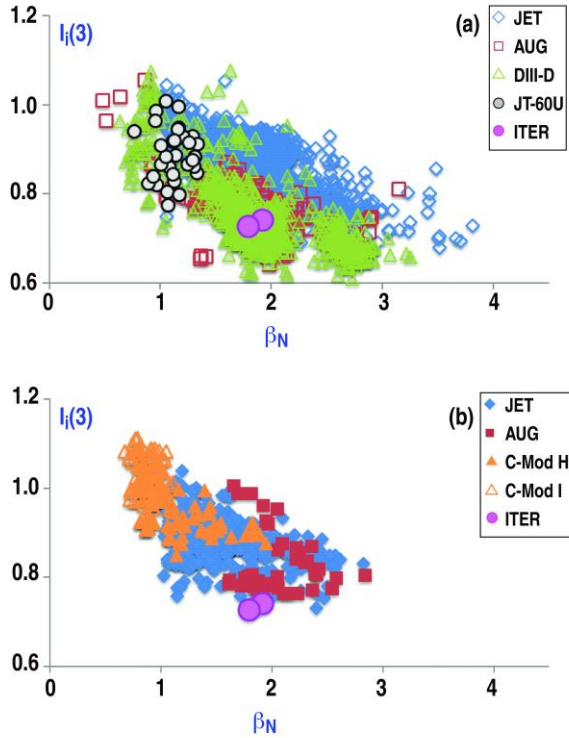

Figure 20: *Comparing the operating space for devices with a carbon wall (top) and metal wall (bottom); the plasma inductance ($l_i(3)$) as a function of normalised plasma beta (β_N). Devices with a carbon wall (top) and metal wall (bottom).*

Experiments with a carbon wall can achieve these low values for $l_i(3)$ as shown in Figure 20. The lower values of $l_i(3)$ at higher beta reflect an increase in bootstrap current contribution due to the edge pedestal. Recent experiments at JET with the Be/W wall found [55] that at high collisionality a lower pedestal pressure is observed. The reduction of the pedestal pressure is associated with an increase in pedestal width, a decrease of the bootstrap current and increase of the relative shift between the positions of the pedestal density and pedestal temperature are observed at JET [56] and AUG [57]. The data from high-Z metal wall devices lie above the ITER flat top predictions of $l_i(3) \sim$ 0.73, even discharges at the highest β_N values achieved in AUG and JET only approach $l_i(3) = 0.75$. The data may indicate that it could be challenging to obtain the predicted (and required) edge pedestal

pressure in ITER with a Be/W wall, but care should be taken comparing $l_i(3)$ values for different plasma shapes. Moreover, the plasma inductance is not a measure of the pedestal pressure, for this the dataset needs to be extended to include pedestal values for plasma density and temperature.

The data show that values of $\beta_N \sim 3$ can be achieved in stationary conditions at $q_{95} = 2.7$ to 3.3 for a range of devices (AUG, JET and DIII-D). More data are available at high plasma beta for experiments with a carbon wall, but there seems to be no difference in plasma MHD stability related to the use of different wall materials. The database does not document the limiting events to the β_N values that can be obtained. H-mode discharges at $q_{95} \sim 3$ limited by the appearance of an n = 1 tearing instability, after the discharge has run at constant pressure for several confinement times, are reported from DIII-D [58]. The database presented here however does not contain MHD onset data to provide a survey across several devices. Experimental values of the stationary H-modes included in the database certainly exceed the values required for ITER ($\beta_N = 1.8$), showing that with potentially more favourable energy confinement at high beta (compared to IPB98(y,2) scaling), or with an increase of additional heating power, ITER could obtain Q > 10. Hence, the performance of ITER can be improved significantly; in terms of fusion power, $P_{fus} \propto \beta_N^2/q_{95}^2$ or duration by operating at higher average plasma temperatures and higher bootstrap current fractions ($\propto q_{95}/\beta_N$).

A dimensionless parameter G that contains the key physics scaling is the figure of merit related to fusion energy gain and can be used to compare the potential fusion performance across tokamaks with different size and magnetic field [59].

$$G \equiv H_{89P}\, \beta_N/q_{95}^2 \qquad\qquad\qquad\qquad (12)$$

Here H_{89P} is the ratio of the global energy confinement (τ_E) to an L-mode scaling [60] and is used to more easily relate confinement and stability. G should be 0.42 for Q = 10 in ITER. As shown in Figure 21, G spans a range of 0.15 to 0.55 at the ITER reference beta of $\beta_N = 1.8$ for carbon wall data, while for data obtained with metal walls G varies from 0.1 to 0.36 (at $\beta_N = 1.8$). Although Figure 21 plots G

against β_N, which is used in defining G, it does show significant variation of G for a given β_N value due

to variation of $\left(H_{89P}/q_{95}^2\right)$, as there are q₉₅ variations within the range 2.7 to 3.3 in the database,

but more importantly because of variations in energy confinement with β_N. Also, there is a marked

difference between carbon wall devices and high-Z metal wall devices in that G ≥ 0.4 is only obtained

for β_N > 2 for high-Z metal wall devices, using dominant co-current NBI heating (AUG and JET). The

figure of merit G uses the total plasma energy, including the fast particle pressure W_fast. Only

discharges with carbon walls can obtain W_fast more than 20 % of the total stored energy (W).

However, analyses of the data show that the best performance is obtained for W_{fast}/W in the range

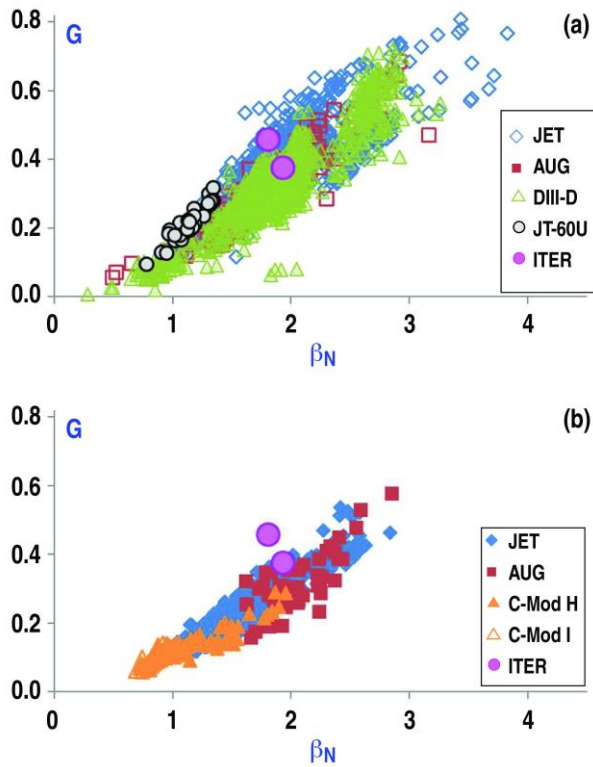5 - 20 %, which is the predicted fast particle content of ITER plasmas.

Figure 21: *Comparing the "figure of merit", as given in Eq (14), for devices with a carbon wall (top) and metal wall (bottom) as a function of normalised plasma beta (β_N).*

The objective of achieving Q = 10 in ITER at 400 - 500 MW of fusion power seems achievable as

shown by the simulations provided by the ITER team. Moreover, the data from devices with carbon

walls show that this objective could even be exceeded with the heating power available at ITER.

However, as shown in Figure 21, only the very best discharges from high-Z metal wall devices achieve

ITER requirements. This is demonstrated in more recent results with the Be/W wall at JET, not part of

the database as entries are restricted up to December 2014, to allow sufficient time for publication of the data. JET obtained operation at a plasma current of 3 MA at q_{95} = 3, reaching β_N ~ 2.15 and H_{98y2} ~ 1.1 in stationary conditions [61].

9. Discussion

The strongly negative beta dependence is a general feature of most energy confinement scaling laws derived from multi-machine databases. A much weaker, in many cases negligible, beta dependence has been observed in dedicated experiments on both DIII-D [34, 62] and JET [36], where β_{th} was varied whilst the other dimensionless parameters were held constant. This discrepancy has been explained in terms of correlations in the multi-machine database, most notably between β and the aspect ratio and differences in the energy transport dependency between core and edge of the plasma. This was illustrated in β scan experiments in H-mode plasmas with type-I ELMs in ASDEX Upgrade, which were at higher collision frequency compared to experiments in DIII-D and JET [63]. These results suggest that degradation of global confinement with β is a plasma edge effect. In addition, non-dimensional transport experiments in JT-60U show a beta degradation of energy confinement. Combining these JT-60U data with subsets of ASDEX Upgrade and JET data in the ITPA H-mode confinement database show that the shaping of the plasma cross section, as well as the fuelling condition of the H-mode discharges are possible candidates for causing the beta dependence of energy confinement, as well as causing variation of the beta dependence among different devices [64].

The disagreement between single scan experiments of the dimensionless parameters and the scaling expressions based on database analyses for the dependencies on both β and ν_C have been investigated before [65]. Thomsen et al [66] showed that the condition of the datasets used to obtain the ELMy H-mode scaling in the late 1990's, such as the IPB98(y,2) scaling, is critical in view of their sensitivity to errors in the absorbed heating power and stored energy. Moreover, the bias in

ordinarily least squares regression due to measurement errors of the ELMy H-mode database is sufficient to explain the discrepancy in the β and v_c dependences provided that the error on the loss power and thermal stored energy is sufficiently large. In addition, no account is taken of the additional loss terms such as radiation and charge exchange. The analyses of Cordey et al [65] of using a reduced dataset for scaling closer to ITER parameters, has β and v_c dependencies closer to the dedicated dimensionless parameter scan experiments of $\beta^{0.0}$ and $v_C^{-0.3}$, similar to the results reported here.

In obtaining an indication on a dimensional scaling with a minimum number of variables, a similar study for the thermal energy confinement time using only three fit parameters (I_p , P_{loss}, R_{geo}) was performed for the advanced inductive database from the ITPA-IOS TG, concentrating on data at high plasma beta for a range of q₉₅ values, but typically q₉₅ > 3 [26]. The regression for these data obtained $\tau_{scaling}\ [s] = 0.16\ P_{loss}^{-0.67}\ I_p^{1.41}\ R_{geo}^{1.04}$ and only gives a small reduction in the quality of the fit when applied to the dataset at q₉₅ ~ 3, with RMS error = 34 %, compared to the fit given in Eq (10) that obtains RMS error of 30 %. It demonstrates that the principle thermal confinement parameters for 0-D data are similar for the two regimes.

The database presented in this paper contains global scalar variables, no data are available (or included) that separate core and edge or pedestal contributions to plasma confinement. Most devices only give the total radiated power from the plasma without separating bulk and edge or divertor radiation. However, the separatrix crosses the area of strongest radiation, such that realistic assumptions on the radial error of the separatrix itself and on the errors of the radial uncertainty of the power deconvolution give rise to large errors on the power outside the separatrix compared to the total power. Information on the pedestal and an agreed formalism to compute core and edge radiation should be included in future database activities coordinated by the ITPA as it may improve predictions to ITER for core confinement, pedestal pressure, and effect of core or edge radiation on plasma performance.

Concerning core and edge separation for predicting confinement, Cordey et al [67] showed that models for the core and edge can be combined to provide a good fit to the ELMy H-mode database used for the IPB98(y,2) scaling. The resulting two-term scaling expressions are shown to give very similar predictions for the confinement time, in the next step devices such as ITER with a predicted stored energy in the pedestal that is 28 - 50 % of the total stored energy. The scaling of the thermal stored energy of the core plasma with dimensionless variables was found $\left(B\tau_{th} \propto \rho^{*-3.02} \beta_{th}^{0.05} \right)$ to be an almost pure gyro-Bohm form. Maggi et al [68] showed results for a multimachine database for the edge pedestal, with the pedestal top pressure increasing moderately with power in all tokamaks, in broad agreement with the power dependence of the IPB98(y,2) scaling. Also showing a robust correlation between the total and the pedestal thermal stored energy, with the pedestal stored energy between 30 % and 50 % of the total stored energy. The inclusion of data with high-Z wall from more recent experiments, would warrant another analysis of the pedestal and core confinement scaling.

Regarding the total radiated power, the scaling of the thermal confinement does not include the radiated power loss from the bulk of the plasma, nor does the scaling for the H-mode threshold by Martin et al [41] include the radiated power to provide a scaling with $P_{net} = P_{loss} - P_{rad,bulk}$, rather than with P_{loss} only. From the experiments we are unable to judge how radiation changes the confinement properties of the H-mode plasmas and therefore it should not be included in the 0-D consideration of the thermal confinement time. However, in contrast to computations of the normalised confinement in experiments, H_{98y2} in ITER is calculated by subtracting the core radiation from the heating power: $P_{loss} = P_{tot} - (P_{brem} + P_{cycl} + P_{line,core})$ [10, 17]. From the analyses presented in this paper the values $B\tau_{th}$ used in ITER simulations are rather high as can be seen from comparisons with scaling expressions in section 5. The values of τ_{th} used are elevated after correcting the loss power for core radiation, due to degradation of energy confinement with input power, while the experiments did not make this correction. Hence, in predictions for ITER, the core radiation

should not be subtracted in the computation of H$_{98y2}$ or τ_{th} to allow comparisons of the confinement with experimental data.

Even after restricting the dimensionless parameters in the trends shown in Figures 5, 6 and 7 in this paper, substantial variation in the normalised thermal confinement remains at fixed values of any of the dimensionless parameters. This variation may arise from changes not captured by the database, such as the ratio of the ion to electron temperature (T$_i$/T$_e$), E × B shearing of turbulence, magnetic shear in the plasma centre and fast particle fractions. Especially, T$_i$/T$_e$ > 1, plasma rotation and fast particle pressures might influence the results obtained at low collision frequency as they have been obtained at low plasma density with co-neutral beam heating in current day devices. The dataset does contain information on T$_i$/T$_e$ and fast particle stored energy, but not consistently across the five devices to draw any conclusions. More work is needed to broaden the data available q$_{95}$ ~ 3, supported dedicated experiments on electron heating and variations of the torque input as reported by DIII-D [69] and by AUG [70].

Beurskens et al [71] showed that Type I ELMy H-mode operation in JET with the ITER-like Be/W wall generally occurs at lower pedestal pressures compared to those with the full carbon wall and that changes in the pedestal stability may have contributed to the reduced pedestal confinement in JET-ILW plasmas. The data presented in this paper, show that the performance potential of devices with a carbon wall is higher and only the best results from devices with a high-Z wall show that ITER should be able to obtain Q ~ 10 at P$_{fus}$ ~ 500 MW. However, experiments during the last decade have shown a steep learning curve in extending the operational range of discharges at q$_{95}$ ~ 3 in high-Z metal wall devices.

Experimental data from devices with a high-Z wall include a reduced pedestal pressure due to the requirement of gas dosing for preventing tungsten accumulation, by maintaining sufficiently high ELM frequency. Also, in ITER, frequent ELMs will be required for avoiding tungsten accumulation in the plasma core, while ELM mitigation techniques will be required in ITER to prevent excessive heat loads and erosion of the divertor. Preliminary estimates indicate for ELM mitigation a reduction

of the average edge pedestal to 80 % - 90 % of the peeling-ballooning limit, as shown by results from MAST using resonant magnetic field coils [72], unless ELM free regimes can be developed at ITER, like QH-modes in DIII-D [73, 74] or I-mode [22]. The influence on the edge pedestal pressure due to ELM mitigation is not included in the simulations for ITER.

The ITER research plan proposes a phased approach to ITER operation, with system commissioning and experiments in hydrogen and helium before starting active operations in deuterium and deuterium-tritium mixtures. Operation at 15 MA in hydrogen, helium or deuterium will not have alpha power heating of the plasma core and be limited to the maximum additional heating power of 73 MW rather than 140 - 150 MW of heating power at the proposed operating point in deuterium-tritium. Hence, initial operation at 15 MA will be "underpowered" and only be able to access H-mode plasmas in deuterium (and possibly in helium) with moderate plasma density (n_e ~ 0.5 n_{GW}) at lower β_N ~ 1 and at low pedestal pressure. The data presented here show that the confinement compared to IPB98(y,2) scaling may be well below H_{98y2} ~ 1 at these values of beta, especially for a high-Z metal wall. The ITER Research Plan should be structured to determine the confinement capabilities at 15 MA and to assess plasma stability at q_{95} ~ 3 and higher β_N together with the performance potential from experiments at reduced plasma current and field. Moreover, during the active phase, deuterium-tritium operation should be started as soon as possible to use the extra power provided by alpha heating.

10. Summary and main conclusions

A database with global parameters of stationary H-mode discharges at q_{95} = 2.7 - 3.3 with data from AUG, C-Mod, DIII-D, JET and JT-60U provides a unique overview of the operational range of the baseline scenario proposed for ITER.

Sufficient data are obtained to study plasma confinement trends with proxies for the dimensionless variables, such as normalised gyro-radius ($\tilde{\rho}^*$), collision frequency ($\tilde{\nu}_C$) and beta ($\tilde{\beta}_{th}$),

with one dimensionless variable while restricting the range of the other two. The ITER values for $\tilde{\rho}*$ are significantly lower than the existing dataset, while ITER values for $\tilde{\nu}_C$ are obtained in experiments today and ITER values for $\tilde{\beta}_{th}$ have been exceeded (Figure 4). The data show trends of $B\tau_{th}$ with $\tilde{\rho}*$ between gyro-Bohm $\left(\tilde{\rho}*^{-3}\right)$ and Bohm dependence $\left(\tilde{\rho}*^{-2}\right)$. Discharges at the lowest values of $\tilde{\nu}_C$ show confinement trends closest to gyro-Bohm scaling (Figure 5), the dataset does have values for $\tilde{\nu}_C$ that approach ITER values only for discharges obtained with carbon walls. Devices with high-Z metal walls have (so far) not found a way to access the low collision frequencies routinely. AUG can only achieve low collisionality for a few discharges following a boronisation of the high-Z walls, with the fresh boronisation mimicking a beryllium first wall in ITER. The dependence on collision frequency is weakly negative, with $B\tau_{th}$ increasing at lower $\tilde{\nu}_C$ values (Figure 6). The dependence of $B\tau_{th}$ with beta is not negative as suggested by the IPB98(y,2) scaling (Figure 7). A good fit to the trends is no dependence on beta ($\tilde{\beta}_{th}{}^0$). Hence, the IPB98(y,2) scaling written in dimensionless form $\left(B\tau_{th} \propto \rho*^{-2.69} \beta_{th}^{-0.9} \nu_C^{0.08}\right)$ does not represent the main trends seen in normalised energy confinement (Figure 8). A pure gyro-Bohm and electrostatic scaling $\left(B\tau_{th} \propto \rho*^{-3} \beta_{th}^0 \nu_C^{-0.14}\right)$ gives a better correlation with the data (Figure 8).

The IPB98(y,2) scaling law still provides a reasonable fit the energy confinement time of the data with an RMS error of 28 % (Figure 10). However, the data on stationary H-modes at q₉₅ ~ 3, restricted to five devices (AUG, C-Mod, DIII-D, JET and JT-60U), the IPB98(y,2) shows significant residual trends in plasma confinement for the four main variables I_p, P_{loss}, R_{geo} and n_e, especially for the plasma density (Figure 11). Improvement of confinement with density is not supported by results from high-Z metal wall devices. Using all the variables employed in IPB98(y,2) results in an overfit due to the correlations among the data (Table III). Moreover, most of the information contained in only three parameters I_p, R_{geo} and P_{loss} (Figure 12).

There are significant differences between the results obtained with carbon wall and results obtained with high-Z metal walls. The carbon wall data span a wider operating space, encompassing

and exceeding the ITER reference point of H$_{98y2}$ = 1 and β_N = 1.8 (Figure 13). Also, H-modes obtained with carbon walls can have good thermal confinement (H$_{98y2}$ ~ 1 or higher) at low input power (P$_{in}$/P$_{LH}$ near 1) and at low plasma beta (β_N < 1.8) ((Figure 13).

Due to the too optimistic scaling with density of the IPB98(y,2) scaling, H$_{98y2}$ reduces with increasing Greenwald density fraction, f$_{GW}$ (Figure 14). The required density in ITER of f$_{GW}$ = 0.85 can be obtained for triangularities δ_x (separatrix) in the range 0.2 to 0.45 (Figure 15). The ITER reference configuration has a design value δ_x = 0.49, experiments targeted in obtaining data at q$_{95}$~3 for triangularities > 0.5 at f$_{GW}$ > 0.8 and H$_{98y2}$ > 0.95 are recommended to give more confidence that the required confinement can be achieved at high plasma density in ITER.

AUG and JET with high-Z walls cannot obtain stationary H-modes at low input power without mitigation strategies for avoiding tungsten accumulation, such as gas dosing for maintaining high enough ELM frequency with low tungsten sputtering. Hence, H$_{98y2}$ = 1 is only obtained at β_N ~ 2 or higher, with P$_{in}$/P$_{LH}$ ~ 2 (Figure 16). H$_{98y2}$ ≥ 1 can be obtained in discharges with dominant RF heating for the full range of $P_{RF}/(P_{NB} + P_{RF})$ from 0 % to 100 % (Figure 17).

Bulk radiation fractions observed in both carbon and metal wall devices are similar to ITER simulations (Figure 18). However, the simulation provided for ITER, when normalised to plasma volume, indicate a much lower core impurity content than observed in experiments at AUG, C-Mod, DIII-D, JET and JT-60U at similar densities (Figure 19). Similar to the conclusions by de Vries at al [49] for the termination phase of ITER, it is not evident that the values in modelling the ITER baseline scenario are done self-consistently with tungsten sputtering and impurity screening in the scrape-off layer and divertor plasma. Assuming higher levels of impurities and radiation may, however, significantly increase the radiative power fraction and reduce fusion performance in ITER. Nonetheless, the core radiation should not be subtracted for calculating the thermal confinement time in ITER, to allow fair comparisons with experimental data from other devices.

Plasma inductance values obtained in today's devices for both carbon and metal walls, lie within the specified range for the ITER poloidal field coils for 15 MA operation ($0.6 < l_i(3) < 1.2$), indicating that the poloidal field coil set is well suited for the mission of ITER (Figure 20). Only the best discharges with high-Z metal walls obtain the ITER performance requirements (Figure 21). The figure of merit G ~ 0.4 required for Q ~ 10 in ITER has only been obtained at $\beta_N > 2$ in high-Z metal wall devices.

The data with carbon wall spans three decades of research and progress is still being made in exploring and expanding the operation space in devices with high-Z walls. However, access to burn in deuterium-tritium plasmas in ITER is certainly going to be more challenging with a tungsten divertor compared to a carbon divertor, especially as at the start of the main heating ITER will have conditions of low input power and low density (for H-mode access) before the alpha power dominates. Moreover, requirements for ELM mitigation and tungsten accumulation may lead to poorer H-mode confinement H_{98y2} ~ 0.8 - 0.9 at $\beta_N < 1.8$. From the data presented here, it is likely that in ITER the energy confinement time will not increase with plasma density and will have no degradation with plasma beta. These observations should be used in simulations for ITER, rather than assuming $H_{98y2} = 1$. The implications of this reduced confinement for tungsten divertor operation together with the lack of beta dependence of the energy confinement on the required additional heating to meet the ITER high Q objectives in the DT phase need to be assessed.

The database presented here could be improved by a better separation of the core and pedestal region for the stored energy and radiation of the plasmas. Nevertheless, the current database represents a wealth of data for the ITER baseline, collected by the IOS TG of the ITPA. The analyses and projections discussed here indicate that operation at 15 MA at q_{95} ~ 3 in ITER can fulfil the primary objective of Q = 10 operation at 500 MW fusion power for 400 s to 500 s, while guiding further experiments and simulations for ITER.

References

[1]   Campbell D.J. and ITER Collaborators," Challenges in Burning Plasma Physics: the ITER Research Plan", *Proc. 24th Int. Conf. on Fusion Energy, San Diego, USA, 2012 (Vienna, IAEA) **ITR/P1-18**.*

[2]   Shimada M. *et al* 2007 *Nucl. Fusion **47 S1***

[3]   Neu R. *et al* 1996 *Plasma Phys. Control. Fusion **38 (1996) A165***

[4]   Urano H. *et al* 2002 *Nucl. Fusion **42 76***

[5]   Neu R. *et al* 2013 *Journal of Nuclear Materials **438 S34–S41***

[6]   Hutchinson I.H. *et al* 1994 *Physics of Plasmas **1 1511***

[7]   Lipschultz B. *et al* 2006 *Physcis of Plasmas **13 056117***

[8]   Matthews G.F. *et al* 2013 *Journal of Nuclear Materials **438 S2–S10***

[9]   Luce T.C. *et al* 2004 *Physics of Plasmas **11 2627***

[10]   ITER Physics Expert Groups on Confinement and Transport and Confinement Modelling and Database, ITER Physics Basis Editors 1999 *Nucl. Fusion **39 2175***

[11]   Sips A.C.C. *et al* 2015 *Physics of Plasmas **22 021804***

[12]   Sips A.C.C. *et al* 2009 *Nucl. Fusion **49 085015***

[13]   Kessel C.E. *et al* 2009 *Nucl. Fusion **49 085034***

[14]   Jackson G.L. *et al* 2009 *Nucl. Fusion **49 115027***

[15]   Greenwald M. 2002 *Plasma Phys. Control. Fusion **44 R27-R80***

[16]   Troyon F. *et al* 1984 *Plasma Phys. Control. Fusion **26 209***

[17]   Kim S.H. *et al* 2015 "Simulating Burning Plasma Operation in ITER", *Proc. 42nd EPS Conf. on Plasma Physics (Lisbon) vol 39E **P4.170***

[18]   Kavin A.A. *et al* 2013 "15 MA DT Scenarios with the CS design and location of the first wall 'Baseline 2012' (C – impurity, the longest burn, control of upper outer strike point on BM#8)"*(May 2013)*

[19]   Schweinzer J. *et al* 2016 *Nucl. Fusion **56 106007***

[20]   Whyte D.G. *et al* 2010 *Nucl. Fusion **50 105005***

[21]   Hughes J.W. *et al* 2013 *Nucl. Fusion **53 043016***

[22]   Hubbard A.E. *et al* 2016 *Nucl. Fusion **56 086003***

[23]   Doyle E.J. *et al* 2010 *Nucl. Fusion **50 075005***

[24]   Nunes I. *et al* 2016 *Plasma Phys. Control. Fusion **58 014034***

[25]   Beurskens M.N.A. *et al* 2013 *Nucl. Fusion **53 013001***

[26]   Luce T.C. *et al* 2014 *Nucl. Fusion **54 013015***

[27]   Luce T.C. *et al* 2008 *Plasma Phys. Control. Fusion **50 043001***

[28]   Kadomtsev B.B. 1975 *Fiz. Plasmy **1 531** [Soviet J. Plasma Phys. **1 295**]*

[29]   Connor J.W. and Taylor J.B 1977 *Nucl. Fusion **17 1047***

[30]   Connor J.W. 1988 *Plasma Phys. Control. Fusion **30 619***

[31]   Horton W. *et al* 2003 *New J. Phys. **5 14***

[32]   Taroni A. *et al* 1994 *Plasma Phys. Control. Fusion **36 1629***

[33]   Erba M. *et al* 1998 *Nucl. Fusion **38 1013***

[34]   Petty C.C. *et al* 2004 *Physics of Plasmas **11 2514***

[35]   Thomsen K. *et al* 1994 *Nucl. Fusion **34 131***

[36]   McDonald D.C. *et al* 2004 *Plasma Phys. Control. Fusion **46 A215***

[37]   Challis C.D. *et al* 2015 *Nucl. Fusion **55 053031***

[38]   Saibene G. *et al* 2002 *Plasma Phys. Control. Fusion **44 1769***

[39]   Beurskens M.N.A. *et al* 2016 *Nucl. Fusion **56 056014***

[40]   Kallenbach A. *et al* 1999 *Plasma Phys. Control. Fusion **41 B177***

[41]   Martin Y.R. *et al* 2008 *J. of Phys: Conf. Ser. **123 01203***

[42]   Ryter F. *et al* 2013 *Nucl. Fusion **53 113003***

[43]   Maggi C.F. *et al* 2014 *Nucl. Fusion **54 023007***

[44]   Loarte A. *et al* 2014 *Nucl. Fusion **54 033007***

[45]   Kessel C.E. *et al* 2015 *Nucl. Fusion **55 063038***

[46]   Koechl, F. *et al* 2017 *Nucl. Fusion **57 086023***

[47]   Versloot T.W. *et al* 2011 *Nucl. Fusion **51 103033***

[48]   Matthews G.F. *et al* 1997 *J. Nucl. Mater. **241–3 450***

[49]   de Vries P.C. *et al* 2018 *Nucl. Fusion **58 026019***

[50]   Telesca G. *et al* 2000 *Nucl. Fusion **40 1845***

[51]   Devynck P. *et al* 2014 *Plasma Phys. Control. Fusion **56 075026***

[52] Pütterich T. *et al* 2010 *Nucl. Fusion* **50 025012**
[53] Dux R. *et al* 2014, *Plasma Phys. Control. Fusion* **56 124003**
[54] Kim S.H. *et al* 2009 *Plasma Phys. Control. Fusion* **51 105007**
[55] Maggi C.F. *et al* 2015 *Nucl. Fusion* **55 113031**
[56] Frassinetti L. *et al* 2017 *Nucl. Fusion* **57 016012**
[57] Dunne M. *et al* 2017 *Plasma Phys. Control. Fusion* **59 014017**
[58] Turco F. and Luce T.C. 2010 *Nucl. Fusion* **50 095010**
[59] Luce T.C. for the DIII-D Team 2005 *Nucl. Fusion* **45 S86**
[60] Yushmanov P.N. *et al* 1990 *Nucl. Fusion* **30 1999**
[61] Kim H-T. *et al* 2018 *Nucl. Fusion* **58 036020**
[62] Petty C.C. *et al* 1998 *Nucl. Fusion* **38 1183**
[63] Vermare L. *et al* 2007 *Nucl. Fusion* **47 490**
[64] Takizuka T. *et al* 2016 *Plasma Phys. Control. Fusion* **48 799**
[65] Cordey J.G. *et al* 2005 *Nucl. Fusion* **45 1078**
[66] Thomsen K. *et al* 2004 *Proc. 31st EPS Conf. on Plasma Physics (London, 2004) vol 28G (ECA)* **P5.145** CD ROM edition http:eps2004.clf.rl.ac.uk/pdf/P5 145.pdf
[67] Cordey J.G. *et al* 2003 *Nucl. Fusion* **43 670**
[68] Maggi C.F. *et al* 2007 *Nucl. Fusion* **47 535**
[69] Solomon W.M. *for the DIII-D Team* 2017 *Nucl. Fusion* **57 102018**
[70] Sommer F. *et al* 2015 *Nucl. Fusion* **55 033006**
[71] Beurskens M.N.A. *et al* 2014 *Nucl. Fusion* **54 043001**
[72] Chapman I.T. *et al* 2012 *Nucl. Fusion* **52 123006**
[73] Garofalo A.M. *et al* 2011 *Nucl. Fusion* **51 083018**
[74] Chen Xi *et al* 2017 *Nucl. Fusion* **57 022007**